ABSTRACT

Title of Thesis: INDIUM PHOSPHIDE MEMS CANTILEVER

WAVEGUIDES FOR CHEMICAL SENSING

WITH INTEGRATED OPTICAL READOUT

Degree Candidate: Nathan Paul Siwak

Degree and Year: Masters of Science, 2007

Thesis Directed By: Dr. Reza Ghodssi, Electrical and Computer

Engineering

This thesis presents the development towards an integrated, monolithic, micro-electro-mechanical system (MEMS) cantilever waveguide resonator chemical sensor using the III-V semiconductor indium phosphide (InP). Waveguide cantilevers with resonant frequencies as high as 5.78 MHz, a quality factor of 340, and a sensitivity of 4.4×10^{16} Hz/g are shown for the first time in this system. The first demonstration of vapor detection using the sensor platform is performed utilizing an organic semiconductor Pentacene absorbing layer. Vapors are measured from mass shifts of 6.56×10^{-14} and 7.28×10^{-14} g exhibiting a mass detection threshold of 5.09×10^{-15} g. The design, fabrication, and testing of an integrated waveguide PIN photodetector with an $In_{0.53}Ga_{0.47}As$ absorbing layer is reported. Dark currents as low as 8.7 nA are measured for these devices. The first demonstration of a resonating cantilever waveguide measurement is also performed using the monolithically integrated waveguide photodiodes with uncertainty of less than \pm 35 Hz. Finally, a future outlook is presented for this monolithic InP sensor system.

INDIUM PHOSPHIDE MEMS CANTILEVER WAVEGUIDES FOR CHEMICAL SENSING WITH INTEGRATED OPTICAL READOUT

By

Nathan Paul Siwak

Thesis submitted to the Faculty of the Graduate School of the University of Maryland, College Park, in partial fulfillment of the requirements for the degree of

Master of Science

2007

Advisory Committee:

Professor Reza Ghodssi, Chair

Professor Christopher Davis

Professor Neil Goldsman

© Copyright by

Nathan Paul Siwak

2007

Dedication

To my family for their never-ending support, to the love of my life for being the most encouraging and patient person I know, and to the One responsible for all my talents and accomplishments, whom without I would be nothing.

Acknowledgements

The author would like to thank Professor Reza Ghodssi for his guidance and support throughout this degree process, and the members of the advisory committee for their helpful suggestions and discussions.

Dan Hinkel, Scott Horst, and Warren Berk for their help with fabrication, and the many hours of informative and indispensable discussions, assistance, and equipment access during the fabrication of the work presented here.

To the researchers in the Molecular Beam Epitaxy (MBE) laboratory at the Laboratory for Physical Sciences (LPS), S. Kanakaraju and Chris Richardson for their assistance in growing and providing MBE samples for these devices, as well as their advice and thoughtful comments.

The LPS and all of the members of the cleanroom staff, Toby Olver, Lisa Lucas, Steve Brown, and Russell Frizzel for their assistance in device fabrication procedures and for the many hours of cleanroom training.

Vince Ballarotto, Dan Hines, and Ellen Williams for their introduction into Pentacene and polymer processing, specifically Vince for his many hours performing Pentacene depositions and Dan for his helpful comments and suggestions.

The members of the MEMS Sensors and Actuators Laboratory for their useful discussions, suggestions, and support, particularly Mike Fan and Jonathan McGee for their many late nights and hard work.

Funding support from the National Science Foundation CAREER Award program, and the LPS 3DI Program (P.I. Dr. Neil Goldsman).

Table of Contents

Dedication	ii
Acknowledgements	iii
Table of Contents	iv
List of Tables	viii
List of Figures	ix
1 Background and Motivation	1
1.1 Thesis Introduction	1
1.2 History of MEMS Technologies	1
1.3 Optical MEMS	4
1.3.1 Free-Space MOEMS	4
1.3.2 Guided MOEMS	8
1.4 III-V MOEMS	10
1.5 MEMS for Sensing Applications	14
1.5.1 Competing Technologies	15
1.5.2 Micromechanical Resonator Sensors	16
1.5.3 Cantilever Readout Methods	18
1.5.4 Absorbing Layers	20
1.6 III-V Integrated Photodetectors	22
1.7 Thesis Organization	24
2 Design	26
2.1 Cantilever Sensing Theory	26
2.1.1 Mass Loading Measurement	26

2.1.2	Mass Sensitivity	27
2.2	Cantilever Waveguide Design	28
2.2.1	Electrostatic Actuation Modeling	29
2.2.2	Optical Coupling Modeling	34
2.2.3	Cantilever Geometries	37
2.2.4	Layer Structure Design	38
2.2.5	Cantilever Mask Design	39
2.3	Waveguide Integrated PIN Photodetector Design	41
2.3.1	Photodetector Modeling	42
2.3.2	Photodetector Layer Structure Design	46
2.3.3	Photodetector Mask Design	47
2.3.4	Photodetector Geometries	49
3 Fabrio	cation	53
3.1	Cantilever Waveguide Fabrication	53
3.2	Photodetector Fabrication Modifications	59
3.2.1	Metal layers	59
3.2.2	Backside Contacts	59
3.2.3	Release Etch	60
3.3	Pentacene Morphology Characterization	62
3.3.1	Initial Film Deposition	63
3.3.2	Deposition on Cantilever Devices	67
4 Testin	ng	71
4.1	Cantilever Waveguide Testing Setup	71

4.2	T	Testing Setup for Vapor Sensing	. 73
4	1.2.1	Environmental Enclosure	. 73
4	1.2.2	Vapor Introduction	. 74
4.3	N	Measurement Methods	. 76
4	.3.1	Cantilever Waveguide Measurement	. 76
4	1.3.2	Data Acquisition	. 79
4	1.3.3	Cantilever and Detector Biasing Schemes	. 82
4.4	R	esults	. 84
4	4.4.1	Cantilever Waveguides	. 84
4	4.4.2	Cantilever Waveguide Vapor Sensing	. 85
4	1.4.3	Integrated Photodetector Results	. 86
4	1.4.4	Summary	. 90
5 Γ	Data A	Analysis and Discussion	. 91
5.1	R	esonant Frequency Analysis	. 91
5.2	F	requency Shift Analysis	. 93
5	5.2.1	Exponential Fitting	. 93
5	5.2.2	Calculated Mass Absorbed / Desorbed	. 93
5.3	Г	Discussion	. 95
5	5.3.1	Cantilever Resonators	. 95
5	5.3.2	Vapor Sensing	. 96
5	5.3.3	Integrated PIN Photodiodes	. 98
6 (Concl	usions and Future Work	102
6.1	S	ummary of Results Reported	102

6.2 Future Work	103
6.2.1 Layer Structure Modifications	103
6.2.2 Functionalization and Absorbing Layers	104
6.2.3 Optical Source Integration	105
6.3 Conclusion	106
Appendix A	108
Appendix B	113
Appendix C	119
Appendix D	120
Bibliography	126

List of Tables

Table 2.1 Sample of cantilever geometries and calculated design parameters	38
Table 2.2 Photodetectors with straight waveguides. All values are present for wavegide widths	
Table 2.3 Photodetectors integrated with cantilevers.	51
Table 4.1 Selected testing results from cantilever waveguides.	84
Table 5.1 Fitting results from exponential models	93
Table 5.2 Calculated values for frequency and mass shifts as well as uncertainties these values	
Table 5.3 Parameters and expressions used to calculate absorbed/desorbed mass	95

List of Figures

Figure 1.3.1 Schematic representation of MOEMS beam steering switch and a top down image [11]
Figure 1.3.2 Lucent WaveStar LambdaRounter TM [4]
Figure 1.3.3 Texas Instruments DMD TM [6]
Figure 1.3.4 Example of waveguide switches in GaAs from [14]
Figure 1.3.5 A waveguide switch fabricated in InP [15].
Figure 1.4.1 Diagram showing the relationship between material composition, lattice constant, and bandgap for some common III-V compound semiconductors [22] 12
Figure 1.4.2 Out of plane electrostatically tuned Fabry-Perot filter in InP [25] with a) SEM showing a device, and b) Schematic design
Figure 1.5.1 Cantilever waveguide principle of operation
Figure 1.6.1 Illustration of differences between a standard surface illuminated photodiode and a side-illuminated PIN waveguide integrated photodiode
Figure 2.2.1 Schematic of device components. Inset: operational principle of the readout mechanism.
Figure 2.2.2 Diagram illustrating parameters relevant to the derivation using the Euler beam equation
Figure 2.2.3 Plot of maximum displacement versus length of cantilever for a variety of cantilever widths, with a cantilever thickness of 2 μ m
Figure 2.2.4 Pull in voltage versus length for two different actuation gap widths 34
Figure 2.2.5 Diagram showing relevant dimensions and features for Gaussian beam propagation calculations
Figure 2.2.6 Percentage optical coupling loss versus cantilever misalignment (in meters). Superimposed is the 5% limitation, showing intersection at approximatley 200 nm
Figure 2.2.7 Diagram of layer structure for cantilever waveguide resonators 39
Figure 2.2.8 0.6 µm cantilever mask layout. Grey areas are metal and red are waveguide definitions. 40

Figure 2.2.9 1.4 µm cantilever mask layout. Grey areas are metal and red are waveguide definitions
Figure 2.2.10 Full die image of cantilever waveguide devices red is unetched InP. Grey is metal deposition
Figure 2.3.1 Numerical calculations of absorption versus absorbing layer thickness adapted from [74] for two radiation wavelengths in an InP/InGaAs/InP PIN photodiode
Figure 2.3.2 Diagram of simulation schematic with relevant items labeled
Figure 2.3.3 Simulation results showing resistive heating and transmitted optica power versus InGaAs thickness
Figure 2.3.4 Two simulation results showing optical power density in two different designs, 1.8 μm absorbing layer and 2.0 μm absorbing layer
Figure 2.3.5 Revised layer structure for the integrated photodetectors
Figure 2.3.6 Mask design of detector regions. Under the same undercut etch, the photodetector region will remain, while the thin waveguide region will be released completely.
Figure 2.3.7 Mask image of cantilever integrated with waveguide with components labeled
Figure 2.3.8 Full die image of integrated photodetector devices mask
Figure 3.1.1 SEM of an InP etch showing "scalloped" sidewall due to the cyclic etching process
Figure 3.1.2 SEM of profile after a cleave has been carried out. The layer structure is visible in this image.
Figure 3.1.3 Image of waveguide facet after critical point drying, showing complete release and undercut of InGaAs.
Figure 3.1.4 SEM of 1.0 μm wide, 30 μm long suspended cantilever resonator 58
Figure 3.1.5 SEM of released cantilever, 75 μm long 1 μm wide
Figure 3.2.1 Optical microscope image of metal pads delaminating after immersion in HF containing solution
Figure 3.2.2 SEM image of destroyed cantilever. 61
Figure 3.2.3 SEM showing successfully fabricated cantilever and photodetector devices.

Figure 3.3.1 SEM profile image of substrate with deposited Pn with measured thickness
Figure 3.3.2 a)VEECO optical profilometer scan of Pn deposition on InP created with a shadow mask, and b) contact profilometer scan of the same step
Figure 3.3.3 SEM image showing an edge of the masked region on a flat InP substrate
Figure 3.3.4 Input waveguide facet showing ~200 nm Pn deposition on the surface and nucleation on the facet
Figure 3.3.5 Top-down image of 45 µm long cantilever after Pn deposition, showing all features intact.
Figure 3.3.6 Input waveguide facet at an angle showing masking effect due to highly directional deposition
Figure 3.3.7 Resonant frequency with and without pentacene
Figure 4.1.1 Testing setup block diagram
Figure 4.2.1 Photograph of device under test showing vapor delivery system 75
Figure 4.2.2 Flask containing liquid (IPA) to introduce vapors to device
Figure 4.3.1 Illustration of how cantilever (dimensions 30 μm long, 1 μm width) response shown by high speed detector (HSD) voltage increases off and on resonance; a) off resonance, 700KHz, and b) on resonance, 758.8KHz
Figure 4.3.2 Ringing measurement of cantilever (dimensions 55 μm long, 1 μm wide). a) Raw ringing data and b) FFT of data
Figure 4.3.3 LabView interface for frequency sweeping program
Figure 4.3.4 LabView interface for the ringing data save program
Figure 4.3.5 Photodiode measurement and simultaneous cantilever actuation schematic. Resistor in the transimpedance amplifier is set at $102 \text{ K}\Omega$
Figure 4.4.1 Plot of frequency versus time experienced during successive IPA introductions
Figure 4.4.2 Plot of resonant frequency versus time during successive EtOH introductions
Figure 4.4.3 a), b), and c) Photo current and Dark current for the 3 waveguide widths and various detector sizes listed by their widths (w) and lengths (l). Each bar

represents a different device described by its width (w) and length (l) in microns. Outlier data points in b) and c) are due to fabrication imperfections
Figure 4.4.4 Underdamped response of 100 µm cantilever waveguide measured using the integrated PIN photodiode.
Figure 4.4.5 Underdamped response of 50 µm cantilever waveguide measured using the integrated PIN photodiode.
Figure 5.3.1 Illustration of frequency tuning effect. Resonant frequency versus applied actuation voltage
Figure 6.2.1 Illustration of how inserting an additional n-type layer into the epitaxial growth would isolate the detector and actuator regions electrically
Figure 6.2.2 Schematic of fully integrated chemical sensor system in InP

1 Background and Motivation

1.1 Thesis Introduction

This thesis will present the development of an InP based cantilever waveguide chemical sensor platform. The first characterization of these cantilever waveguide sensors has been carried out, optimizing device dimensions and establishing a robust testing and measurement procedure. With an established infrastructure, an active absorption layer of the organic semiconductor Pentacene (Pn) has been deposited on the cantilevers in order to perform the first absorption measurement of chemical vapors. Validation of chemical sensing is the first benchmark in determining the real-world sensitivity and repeatability offered by these devices.

A second goal of this thesis is to present the design, fabrication, and testing of a waveguide PIN photodetector integrated with a cantilever waveguide chemical sensor. The testing of photodetectors and cantilever waveguide elements have performed separately before integrating them together and developing a dedicated testing scheme. The integration of a monolithic active optical element in the cantilever waveguide platform will be presented as an illustration of the capabilities of this fabrication method and sensor design which shows its advantages over traditional systems.

1.2 History of MEMS Technologies

Micro-electro-mechanical Systems (MEMS) are traditionally described as the integration of mechanical elements with electronics on the microscale. In most

systems, electronic components interact with the environment through the use of external sensors and actuators. Separate systems need to be connected using various packaging techniques. While these methods are robust and effective, future interconnects will undoubtedly introduce parasitic effects as circuits and electronic equipment continue to be miniaturized. This can decrease the device's overall sensitivity. MEMS technology aims to combat this problem by decreasing sensors to the IC dimensions to ease packaging considerations and decrease parasitic capacitance and resistance that often lead to reduces sensitivity and increased power consumption. Furthermore, MEMS are designed to take advantage of the IC fabrication industry by integrating the sensors and actuators directly on chip with circuitry.

In addition to the connectivity benefits, IC fabrication technology allows for high density batch fabrication to be realized. This greatly reduces the cost of sensors, increase the sensor reliability, and will decrease assembly complication. All of these factors make MEMS sensors more attractive than their macro counterparts [1]. Due to their small size, a number of sensing or actuating functions can be integrated monolithically in the same device, further reducing cost, chip size, and increasing functionality [2]. There have been a number of MEMS commercialization successes, most notably accelerometers, gyroscopes, projection systems, and pressure sensors [3]. These examples have all benefited from the high throughput batch fabrication and increased functionality due to the devices' foundation on IC fabrication technologies. The MEMS mechanical elements are fabricated using techniques common with standard IC fabrication such as lithography and dry etching, however

special processes have been developed to "micromachine" them with similar microfabrication tools. The different fabrication methods are used to make these structures grouped into two basic categories are: bulk micromachining and surface micromachining.

Bulk micromachining indicates that the fabrication process involves removing large portions of the substrate, in most cases silicon, to fabricate the structure. Often wet etching processes are used in bulk micromachining, such as the anisotropic etchants potassium hydroxide (KOH), tetramethylammonium hydroxide (TMAH), and ethylenediamene pyrocatecol (EDP) and the isotropic hydrofluoric, nitric, and acetic acid (HNA) etchant [2]. Anisotropic etchants take advantage of the crystal planes of silicon and etch preferentially in various crystal directions. Isotropic etching does not etch preferably along any crystal plane. These etches are most commonly used to undercut structures to make them free-standing and moveable. In addition to wet etching, some "dry" etching processes have been developed to perform the same tasks. Xenon diflouride (XeF₂) gas is used to etch silicon isotropically. Other fluorine chemistries are used in plasma etching systems to etch isotropically. The Deep Reactive Ion Etching (DRIE) process, however, is a cyclic anisotropic plasma etch.

Surface micromachining processes tend to be more compatible with the traditional IC fabrication processes which involve releasing layers that have been deposited on the substrate. Most commonly surface micromachining is associated with the fabrication of polysilicon structures. A sacrificial layer is deposited on the substrate, most processes use silicon dioxide (SiO₂) due to its high selectivity in a

hydrofluoric acid (HF) etch. On top of the SiO₂ sacrificial layer, a layer of polysilicon is deposited. Once it is deposited, an etch which removes the sacrificial layer but not the polysilicon layer is used to release the devices in the structural layer. Modern accelerometers utilize this fabrication method.

1.3 Optical MEMS

MEMS research has expanded greatly since the early 1980's and has generated a number of specializations, one of which is the field of micro-optomechanical systems (MOEMS). MOEMS are a subset of the MEMS research field which specifically deals with light generation and manipulation using micro structures and elements. As with MEMS technologies, they take advantage of the batch fabrication and parallelism that IC fabrication methods offer. Some of the more common applications for these devices include communications and projection display technologies [4].

These devices can be made of a variety of materials: standard silicon substrates, polymers, or III-V direct bandgap semiconductors such as indium phosphide (InP), gallium arsenide (GaAs), and indium arsenide (InAs) for example. The selection of the materials depends on the application and level of system integration desired. MOEMS can be generalized into two major categories of system architectures: free-space and guided.

1.3.1 Free-Space MOEMS

Free-space MOEMS route and control light by using mirrors and refractive elements. Most examples of free-space MOEMS are optical switches and routers for

communications applications. Characteristically, the free space MOEMS devices are seen as beneficial for very large scale applications such as backbone networks due to their flexibility and scalability with data format and port count. Free-space switches also benefit from high throughput and protocol transparency for transport. Beam routing is a relatively mature segment of MOEMS research, with a variety of designs and devices explored. Many of these designs are simple "on-off" mirrors which block or transmit light; however recent work has concentrated more on beam steering devices [4-6, 7 2003, 2003, 2003, 8-10]. A more recent example of a MOEMS free-space router by Neilson *et al* [11], describes an array of 2-axis beam steering mirrors which have a system of microlenses to help collimate the beams as they are propagated through the system (Figure 1.3.1).

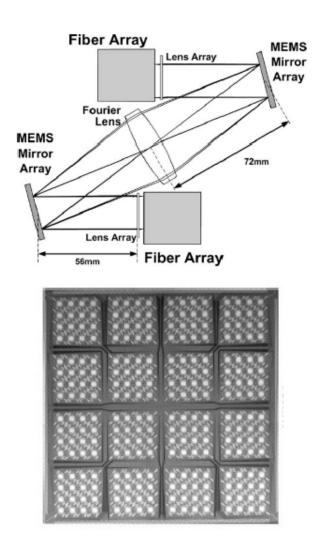


Figure 1.3.1 Schematic representation of MOEMS beam steering switch and a top down image [11].

Part of the importance of this specific device is that it was designed for use with industry standard single mode fibers, which presented a challenge in achieving low loss due to high levels of beam expansion from the single mode fibers. A microlens arrays and other free space optics are essential to achieving the low insertion loss in this system in preventing excessive divergence in the propagating beams. Low insertion loss is also due to the high reflectivity of the micromirrors. A 238×238 port cross connect was demonstrated to meet standard telecommunications performance requirements, exhibiting an average insertion loss of 1.33 dB. These systems do not seem to have seen much widespread use, possibly due to the

complexity involved in fabrication and controlling large numbers of mirrors and accurately. Another drawback to this configuration is crosstalk and losses that can be experienced during beam switching. Notable examples of commercial free-space MOEMS are the LambdaRouterTM [4], and the Texas Instruments Digital Mirror DeviceTM (DMDTM) [6]. The LambdaRouterTM (

Figure 1.3.2) is a predecessor to the devices shown in [11] and in the same way uses arrays of analog, tilt-able, two axis micromirrors to perform non-blocking transmission through free space onto another array of positionable mirrors which then direct the beams to the output port. The Texas Instruments DMDTM (Figure 1.3.3), possibly one of the most famous examples of MOEMS success, is a projection device which uses an array of binary tilting micromirrors to reflect pixels to a screen or surface.

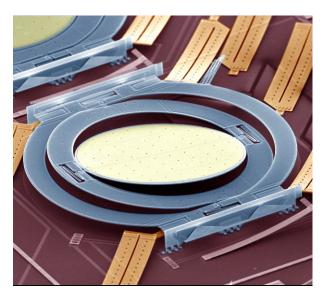


Figure 1.3.2 Lucent WaveStar LambdaRounterTM[4].

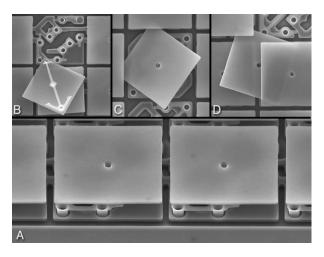


Figure 1.3.3 Texas Instruments DMDTM [6].

Integration of these devices with external components can be difficult due to the inherent out-of-plane operation. Involved packages are needed to fully implement these designs, especially those used for communications applications. This increase in packaging complexity increases future cost, decreases multi-device integration, and limits deployment possibilities.

1.3.2 Guided MOEMS

In an attempt to increase the level of integration available for MOEMS devices, many groups are turning to guided optics instead of the free-space approach. Rather than rely on free space transmission, guided optics use moveable waveguides or optical fibers to control the path of light. Guided optics have more flexibility in controlling the direction of optical propagation since paths are defined lithographically rather than through out-of-plane reflections. This leads to high levels of integration [12] due to this in-plane optical propagation which is easier to package with other components.

Free-space MOEMS often experience less optical loss than the guided MOEMS devices. This is due to the reduced surface roughness of planar surfaces compared to that of etched sidewalls or waveguides in most guided MOEMS, which cause scattering losses. It is also more challenging to achieve high throughput with guided MOEMS devices due to the limited options for reconfiguring optical pathways. While these are both concerns, their importance is offset by the ability to integrate larger numbers of devices together using a lithographically defined

The vast majority of guided MOEMS are optical switch implementations. The basic guided switch consists of moving a waveguide or fiber cantilever and coupling it across a short gap to the intended output. Most of these devices are electrostatically actuated. There have been a number of high throughput switches constructed and proposed using guided MOEMS switches, but due to insertion losses, most require complex solutions like index matching fluids. For example, Ollier *et al* [13] demonstrated seven 1×2 switches which have been cascaded into a 1×8 optical switch. The insertion loss of this device was measured to be 1.5 dB, and was achieved only after using index matching fluid in the gap region over which the light was traveling in free space. 1×2 optical waveguide switches are plentiful in the field of MOEMS, and examples of two of these devices are shown in Figure 1.3.4 and Figure 1.3.5. These two examples utilize III-V compound semiconductors in fabrication, which will be discussed in the next section.

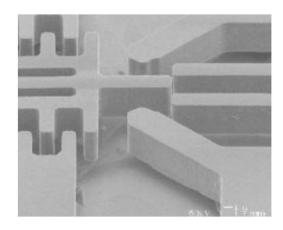


Figure 1.3.4 Example of waveguide switches in GaAs from [14]

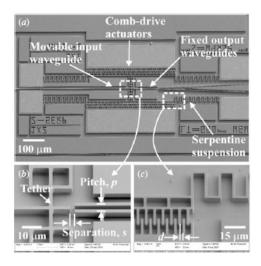


Figure 1.3.5 A waveguide switch fabricated in InP [15].

1.4 III-V MOEMS

Integration of components is critical to the development of MOEMS, as it was in standard MEMS technologies, and serves as the driving force behind much of the research development. The integration of optical components, however, is not as straightforward as the integration of electronic counterparts. Optical components often require a variety of different materials, interconnects, and strict alignment tolerances which increases the complexity of this task. Monolithic integration, which has been demonstrated repeatedly in MEMS, is even more difficult to achieve.

MOEMS devices fabricated from III-V direct-bandgap semiconductors have the distinct advantage to allow both passive and active optoelectronics within a single substrate. Many III-V devices need to be carefully cleaved along crystal planes to create optical quality facets, forcing optical systems to be comprised of a number of die, rather than a single chip. With improved fabrication methods and materials, devices can be created without the need for cleaving; creating new possibilities for monolithic fabrication of MOEMS systems.

III-V materials for MEMS have been pursued for a variety of reasons. The flexibility to specify material properties (stress, bandgap, lattice constant) in compound semiconductor systems is an advantage when using these materials. Etch selectivity between various materials can be established by varying the composition of the grown material thus allowing for the development of etch stops, sacrificial layers, single crystal device layers, and more importantly the ability to fabricate mechanical and optical elements within the same substrate. These properties are made possible through the growth of single-crystal substrates by way of molecular beam epitaxy (MBE) and metalorganic vapor phase epitaxy (MOVPE); two growth techniques developed to precisely control the composition of these compound semiconductors. Examples of materials that can be grown with varying bandgaps and lattice constants is illustrated in Figure 1.4.1. While there have been a number of MEMS devices developed in these III-V material systems which take advantage of tunable piezo properties [16-19], high electron mobility [20], or thermoelectric properties [21], the vast majority of devices take advantage of the tunable optical properties of these materials.

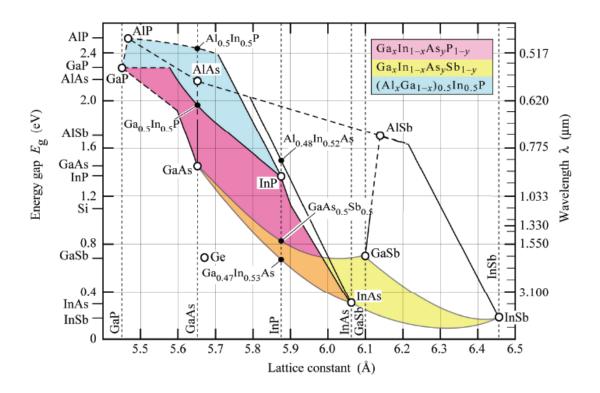


Figure 1.4.1 Diagram showing the relationship between material composition, lattice constant, and bandgap for some common III-V compound semiconductors [22].

A large number of III-V semiconductor compounds are direct-bandgap materials, making them suitable for the generation and detection of light. Furthermore these devices can be grown with variable bandgaps and compositions with the same lattice constant (see Figure 1.4.1), providing for optical, mechanical, and chemical tunability. Various devices can be created by growth of these materials.

The devices shown in Figure 1.3.4 and Figure 1.3.5 utilize the chemical selectivity possible by growing etch selective layers between a bottom substrate and top waveguide layer. Bakke *et al* utilizes GaAs/AlGaAs [14] while Pruessner *et al* uses InP/InGaAs [15]. For each case, the InP and GaAs layers are grown on the top of a single crystal sacrificial layer. Pruessner *et al* also has created other devices such as evanescent couplers using a similar material system [23]. These devices benefit

from the ability to create high-quality, single crystal waveguides by utilizing lattice matched sacrificial layers.

Chemical etching selectivity and atomic-level surface roughness achievable using epitaxial growth techniques has also been used in the fabrication of optical filters and distributed Bragg reflectors (DBR). Tunable filters utilizing Fabry-Perot cavities have been widely implemented [24-28]. One of the more effective methods of filter construction is to make the DBR reflector mirrors in the plane of the substrate (input light is incident perpendicular to the plane of the wafer). Creating the DBR mirrors on the substrate allow for them to be made with very accurate thicknesses and atomic scale roughness through the use of epitaxial growth techniques. DBR stacks with high reflectivity can be realized with this method. A sacrificial material can be grown between subsequent single-crystal semiconductor slabs, which allow for the creation of air cavities to facilitate DBRs and Fabry-Perot cavities. Irmer *et al* [25] demonstrates an example of one of these devices (Figure 1.4.2), and illustrates the wide tunability of these moveable mirror devices (142 nm).

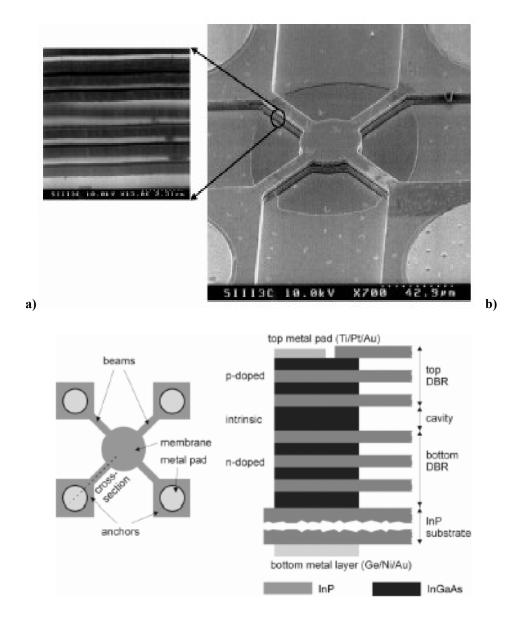


Figure 1.4.2 Out of plane electrostatically tuned Fabry-Perot filter in InP [25] with **a)** SEM showing a device, and **b)** Schematic design.

1.5 MEMS for Sensing Applications

While MEMS technologies have been used for a wide variety of applications, the majority of these devices have focused on interacting with the environment to transduct information from the mechanical to the electrical domain. Devices such as MEMS accelerometers and MEMS pressure sensors are examples of commercial

successes in this area of specialization. Commercial applications aside, research has concentrated on environmental sensing since some of the first micromechanical devices were reported [29, 30].

This thesis also concentrates on utilizing MEMS for sensing applications.

This section comprises a literature review of non-MEMS sensing methodologies and a more detailed discussion of common MEMS sensing techniques.

1.5.1 Competing Technologies

There are a number of existing chemical sensors without micromechanical structures, using capacitive, resistive [31], bulk resonance [32], and optical methods [33] to transduct a chemical response into a useable signal [34]. The performance of these sensors is often limited by large required device sizes, power consumption, and support equipment which can prevent large-scale integration and portability.

Capacitive and resistive chemical sensors have been developed extensively in the past to detect chemicals in both gaseous and liquid forms [34-40]. These types of sensors are usually simple to realize, being an element which measures changes through the variation in resistance or capacitance induced by a chemical reaction or environmental change. Demonstrations of ppm sensitivities are common with these sensors [34]. Sensitivity can vary based upon materials interrogation methods used. While fabrication can be as simple as depositing a polymer on electrodes, this is not readily performed using standard microfabrication techniques. Furthermore, to provide for large changes in resistance or capacitance, devices are usually required to be large. Both of these factors cause the sensors to be difficult to combine in large-

scale arrays that are desired. The sensitivity to humidity can also be troublesome in real-world deployment.

Surface acoustic wave (SAW) resonator sensors [32, 41] measure the resonant frequency changes of a surface/bulk resonator due to surface absorption of the target chemical analytes. Most SAWs are very sensitive due to high resonator quality factors and can be easier to fabricate since they use established fabrication techniques. The drawback of using SAWs lies in their inability to be integrated into a multi-functional system. Devices can be relatively large making them difficult to integrate into a single-chip array, and cross-talk between multiple resonators on the same substrate can cause problems when attempting to perform multiple chemical recognition studies on a single-chip sensor.

Optical sensors operate by using optical fibers or waveguides to collect fluorescence from molecules or to measure index of refraction changes in solutions or gasses that indicate different chemical changes. A number of commercial examples exist which utilize this method of sensing [42, 43]. While they are simple in operational theory and quite sensitive, most of these devices require additional sample preparation and labeling, which reduces their applicability to real-world situations. Many of the commercial and academic examples of these sensors require large external equipment such as lasers, spectrum analyzers, and photodetectors [44-48] which can be a hindrance to sensor deployment.

1.5.2 Micromechanical Resonator Sensors

In contrast to traditional designs, MEMS utilizing mechanical microstructures such as micromachined cantilevers provide promising sensor solutions which are

small, scalable, low power, and ultimately portable. The ability to mass produce and to accurately control and tailor device mechanical properties of such sensors provides a distinct advantage over some non-mechanical approaches.

First demonstrations by Nathanson and Howe [29, 30] using resonant microbridges for filtering and vapor sensing showed the initial promise for these MEMS sensors. MEMS resonant beam and cantilever sensing has since become a well established method to detect various analytes in an environment. Many of these devices have the advantage of performing detection with a label-free method [33, 49] and can be fabricated into arrays to perform multiple sensing operations simultaneously. Recent developments have reported detection of the attachment of single cells, DNA, viruses [50], and even attogram-level mass measurements [51].

Micromechanical resonators have been able to achieve highly sensitive mass measurements while in a vacuum environment, which can be a disadvantage when compared to other sensing methodologies. Operation of these resonators in solution also presents a problem due to the increased viscous dampening experienced in these conditions. This reduces the quality factors of the resonators and makes frequency shifts more difficult to measure. Thus, very few cantilever resonator mass sensors have been demonstrated in fluid environments. While dampening due to ambient air can reduce the sensitivity of the resonator, there have been a large number of examples of micromechanical resonators achieving sufficient sensitivities for their intended applications [52-55]. A feedback measurement system is another solution to increase measurement resolution and artificially "inflate" quality factors of the resonant devices.

1.5.3 Cantilever Readout Methods

A cantilever sensor requires an appropriate measurement system to achieve its maximum potential. A sensitive readout mechanism determines the ultimate detection limit of a system, being able to detect minute changes in resonant frequency or static displacement due to surface stresses.

Traditionally, the most sensitive cantilever sensors have been measured using external optical methods [33, 50, 56, 57]. High displacement resolution allows for lower voltage resonant operation in electrostatically actuated systems and even the possibility of ambient thermal excitation of resonant cantilevers. The most common measurement technique is similar to that employed in atomic force microscopy (AFM) where a laser is reflected off the cantilever surface onto a position sensitive detector (PSD) [55]. Oscillations of the cantilever can be measured by the continuously changing response of the detector. Other optical methods, such as interferometric measurements [58], can be used to achieve ultra-sensitive displacement resolution; however, like AFM techniques, they generally require costly and bulky equipment and infrastructure. Methods, such as piezoelectric [59], piezoresistive [60], and capacitive [53] readout schemes have also been employed to measure cantilever response; however, they do not offer the same benefits of high displacement sensitivity and relative electrical noise immunity that optical methods exhibit [33].

The major drawback in using optical readout methods lies in the large freespace optical components (lasers, alignment mirrors, etc.) required, which limit the deployment of these sensors from laboratory use to portable systems. Furthermore, alignment tolerance and accuracy for these methods can be very stringent, as focusing a laser beam onto a microscale device is difficult. Due to these alignment challenges and the necessary reflected optical signals, cantilever device sizes are constrained to designs which allow the beam to be focused onto the surface, potentially decreasing the sensor sensitivity. To obtain the best displacement resolution, vibration isolation, as well as photodetector and sample thermal stability, become more critical due to the increased degrees of freedom introduced by the large number of components involved in the measurement setup [61]. The need for noise free, sensitive, compact and portable devices, therefore, requires a different readout approach.

The approach used to address these issues is a cantilever displacement readout scheme which relies on the change of optical coupling between two waveguides, shown schematically in Figure 1.5.1. An input waveguide guides coupled laser light through a section of the waveguide that is separated and released from the substrate. As the "free" cantilever waveguide oscillates, it misaligns with a fixed output waveguide, decreasing the optical power coupled to the output waveguide. This output waveguide then guides the light to an additional lensed fiber and then to an off-chip photodetector.

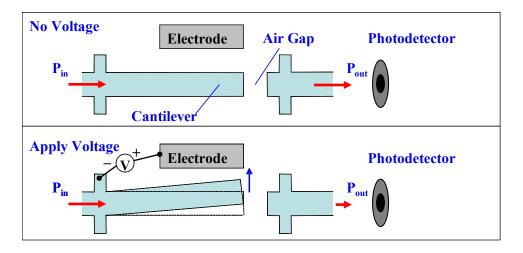


Figure 1.5.1 Cantilever waveguide principle of operation.

This optical coupling due to misalignment provides a very sensitive displacement measurement, with reported displacement resolution comparable to the traditional PSD / reflection readout system ($\sim 20 \text{ fm} / \sqrt{Hz}$) [61]. The complexity and amount of external equipment required is reduced significantly using this method and the alignment procedures for coupling on and off chip are simplified. This concept has been used with silicon dioxide SiO₂ cantilever waveguides for vibration measurements [62] and as a possible replacement for AFM cantilevers in force measurements [61].

1.5.4 Absorbing Layers

Chemical sensors use a variety of selective coatings from polymers to self assembled monolayers (SAMs) [33, 49, 63] to attract chemical species to the active areas of the devices. The vast majority of these coatings are a passive component of the sensor as a whole: a mass absorption or surface stress change is only measured from these layers by the appropriate transducer, and from these effects the chemical is

inferred. To perform the sensing of multiple chemicals in parallel, multiple sensitive layers will be required; which complicates operation and fabrication steps.

Traditional self assembled monolayers (SAMs) are a very common coating to create a functional surface for chemical and biological sensors [33, 2003 Pinnaduwage et al]. The reliable deposition of these films, their ability to be patterned, and their flexibility to be used in a variety of situations has made them a popular choice for chemical coatings. These films are limited to surface adsorption effects, but can be tailored for very specific chemical or biological attachments.

Polymers such as polyethereurethane (PEUT), polyimide, or polycarbosilane [64-66] are often used as chemical sensing layers. These polymers increase mass, volume, or surface stresses depending on the transducer sensing function desired. These materials are often chosen because of their robustness and ease of use. Many of these polymers can be modified in such a way to increase affinity for various chemicals, such as curing them at different conditions, introducing suspensions of other compounds, or by changing the polymer concentration. Due to inherent chemical properties of these layers such as hydrophilicity, polarity, or porosity, they do not exhibit the same type of specific affinities that SAMs provide.

While the two main groups of absorbing layers are passive in nature, active absorption layers have been used in solid state and organic chemical field effect transistors. These Chem-FET sensors [67-71] use mobility and charge changes due to absorption and proximity of chemicals to detect materials of interest. Chem-FETs, just as resistive or capacitive sensors, can be limited by the inability to distinguish between analytes due to similar responses between chemicals. This thesis proposes

an active absorption layer such as those used in Chem-FETs to be implemented on cantilever resonator sensors. The resonators to measure mechanical effects such as mass increase or surface stresses due to the absorption of analytes in these layers, with and electrical changes using an integrated Chem-FET. Functionality of this sort has the potential to increase the selectivity between analytes through multi-modal sensing.

1.6 III-V Integrated Photodetectors

While it has been shown that a number of MEMS technologies exist using III-V semiconductors, these materials have been explored primarily for use in optoelectronics due to their direct bandgap. Creating highly sensitive photodiodes is one of the many conventional applications of these materials. They are ideally suited for use in devices due to their direct bandgap transition, and the ability to control optical characteristics of the materials based upon their compositions.

Silicon photodetectors often suffer from their limited absorption volumes due to restrictive geometries and material properties. Planar diodes located at the surface of a substrate only capture a fraction of the incident photon flux, as the depletion region created in this type of geometry is small. Buried diodes, which have larger depletion regions, experience reduced incident flux due to the slight absorption in the top semiconductor layers before reaching the depletion region. III-V semiconductors along with epitaxial techniques allow semiconductor regions with varying indexes, making the top semiconductor layers of a photodiode to be transparent to the incident radiation, while maintaining the lower semiconductor layers' absorption properties.

Common photodetectors, such as surface illuminated PIN diodes, are made with these materials for this reason.

The major bandwidth limiting factor in surface illuminated PIN photodiodes (see Figure 1.6.1) is the transit time of the photogenerated carriers through the intrinsically doped photon absorption region and to the P and N doped sides of the diode. Reducing the thickness of the absorption layer will clearly decrease the time of transit from the P to the N regions, but simultaneously reduces the absorption crossection encountered by incoming radiation, reducing the responsivity of the photodiode. This raises a clear disadvantage to obtaining high bandwidth and high quantum efficiency simultaneously [72, 73].

"Side illuminated" waveguide PIN photodiodes (see Figure 1.6.1) were introduced to combat this undesirable tradeoff between bandwidth and quantum efficiency [74]. By using a waveguide structure with an underlying absorption region, the thickness of the absorbing region could be reduced without reducing the absorption length of the photodiode. This gives control to the designer over bandwidth and quantum efficiency nearly independent from each other. A number of diodes have been demonstrated with bandwidths in excess of 100 GHz by using this photodetector configuration [72, 73, 75, 76] and even higher bandwidths by using a traveling wave electrode configuration [77, 78].

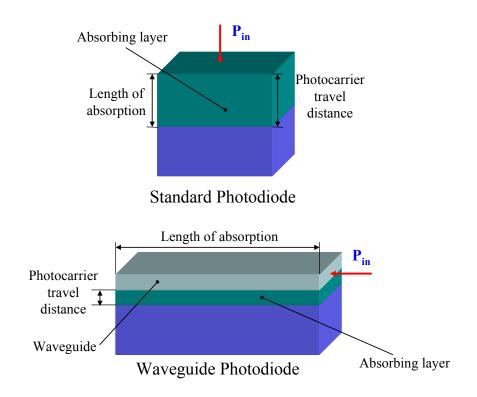


Figure 1.6.1 Illustration of differences between a standard surface illuminated photodiode and a sideilluminated PIN waveguide integrated photodiode.

1.7 Thesis Organization

This thesis is structured as follows: Cantilever sensor theory is presented in Chapter 2, covering the overreaching principles of cantilever resonator sensors. The design of the cantilever waveguides and the integrated PIN diodes with relevant simulations and modeling will be presented in Chapter 3. Cantilever waveguide fabrication procedures with the modifications made to the process flow to fabricate the PIN diodes will be shown in Chapter 4. Testing elements such as setup and experimental procedures with the associated results of cantilever waveguides, vapor sensing, and PIN diode results will be presented in Chapter 5. The data analysis and

further discussion of the results will be given in Chapter 6. Finally Chapter 7 will present a brief summary of the results, future work, and a final conclusion.

2 Design

2.1 Cantilever Sensing Theory

2.1.1 Mass Loading Measurement

As a sensor, micromachined cantilevers are coated with specific receptor or absorption layers which have affinity to a particular analyte in the atmosphere. Chemical or biological agents will absorb into and on top of this coating, changing the mass of the cantilever and producing a resonant frequency shift [33]. This shift can be predicted and used to infer the quantity of absorbed mass

By solving the Euler beam equation for a singly clamped beam, and applying this result to Hooke's law, we can determine an approximate value for the resonant frequency of the structure [33], yielding the well-known equation:

$$f_o = \frac{1}{2\pi} \sqrt{\frac{3EI}{L^3 c_o m_o}}$$
 2.1

where E is Young's modulus, I is the cantilever area moment of inertia, L is the cantilever length, m_o is the cantilever mass, and $c_o = 0.24$ is a mass correction factor for a rectangular beam. This equation can also be expressed in terms of relevant design parameters such as density, width, length, and thickness of the cantilever:

$$f_o = \frac{w}{2\pi L^2} \sqrt{\frac{aE}{\rho}}$$

where w is the cantilever width, L is the cantilever length, ρ is the density of the cantilever material, and a is a geometric factor (140/132 \approx 1.06 for a rectangular cross-section). It is noted that in this and all subsequent equations, that the cantilever

width is defined as the dimension in the direction of motion rather than the thickness, which is a more commonly encountered convention.

By modifying Equation **2.1** to represent the mass of the cantilever and the absorbed mass separately, the shifted frequency due to this additional mass can be shown as:

$$f_{shifted} = \frac{1}{2\pi} \sqrt{\frac{3EI}{L^3(c_A m_A + c_o m_o)}}$$
 2.3

where, m_A is the absorbed mass and c_A is a constant that describes the position of the added mass (0.24 < c_A < 1). Measuring the change in cantilever resonant frequency over time after being exposed to an analyte allows the added mass of the analyte to be calculated using Equation 2.3. Determining this mass shift provides information about the specific chemical or biological agents in the environment.

A frequency shift can also be used in a qualitative fashion by detecting a binary response to various chemicals: an appreciable frequency shift indicates the presence of a chemical species, determined by the absorbing material used. A large array of cantilevers with varying absorbing coatings can be fabricated and calibrated to recognize a particular sensor response to analytes of interest [79, 80]. This approach presents itself as a more useful sensing methodology due to its scalability, relative ease of implementation, and ability to screen multiple analytes simultaneously.

2.1.2 Mass Sensitivity

Resonant frequency of the cantilever waveguides is used as a design parameter due to its relation to the sensitivity of the device. The mass loading

sensitivity can be expressed as the ratio of measured frequency shift to the mass change [33]:

$$\frac{\Delta f}{\Delta m} = \frac{f_o c_A}{m \cdot 0.48}$$

Where m_0 is the cantilever mass, f_0 is the resonant frequency, and c_A is a coefficient from 0.24 - 1 describing the location of the mass attachment (1 = concentrated at the cantilever tip). From Equation **2.4** we see that the sensitivity of the cantilever in question is proportional to the resonant frequency.

Equation 2.2 shows that increasing the width of the cantilever and decreasing the length of the cantilever will increase its resonant frequency, and thus increase the sensitivity of the device as defined in Equation 2.4. Higher resonant frequencies exhibit higher Quality Factors (Q) as dampening coefficients decrease with resonator length [81]. Higher Q factors will lead to more narrow resonance peaks; thus, decreasing the minimum measurable frequency shift (Δf) which influences the minimum detectable mass. It is also noted that the cantilever "thickness" does not play a role in the sensitivity of the device as it does not change the resonant frequency.

2.2 Cantilever Waveguide Design

The cantilever sensor platform presented here operates based upon the optical misalignment principle discussed previously. In addition to this readout mechanism, these devices are designed in the InP III-V semiconductor material system to take advantage of the material flexibility and future monolithic integration as described earlier. The devices presented here aim to combine the advantages of integrated

optical components with the highly sensitive readout mechanism. This section presents background on the specifics of the InP cantilever waveguide resonator which was studied for this thesis. A schematic of the device and operation is shown in Figure 2.2.1.

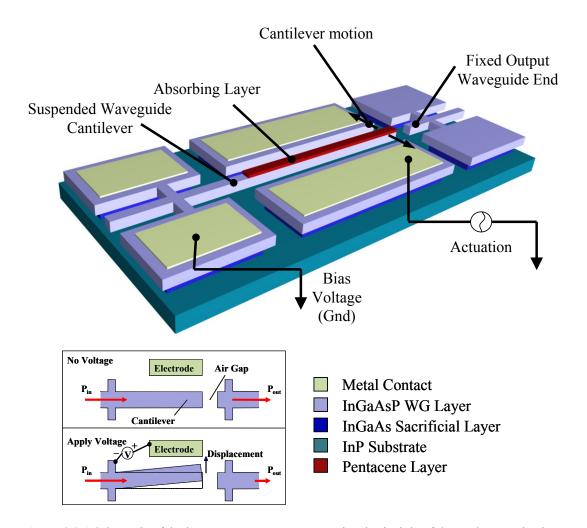


Figure 2.2.1 Schematic of device components. Inset: operational principle of the readout mechanism.

2.2.1 Electrostatic Actuation Modeling

The design of the cantilever waveguides concerned practical considerations of electrostatic actuation, such as the pull-in voltages of the cantilever and the maximum

voltages to be applied the electrodes to actuate the device. This will fundamentally limit the stiffness of the cantilever to values that allow the cantilever to be actuated at this maximum voltage.

Static displacements due to this applied voltage were calculated assuming a uniform electrode and small displacements while assuming the parallel plate capacitor model. Previous experiments using this material layer structure identified a maximum voltage of 26V which could be applied to the InP layer structure before breakdown occurred. This was used as a upper bound for actuation voltage.

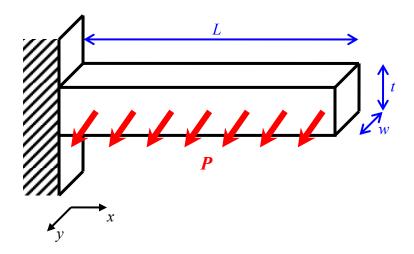


Figure 2.2.2 Diagram illustrating parameters relevant to the derivation using the Euler beam equation. Solving the Euler beam equation (referring to Figure 2.2.2):

$$EI\frac{d^4d(x)}{dx^4} = P$$

where E is the Young's Modulus of the material, d(x) is the displacement of the beam along the x direction, P is the electrostatic force acting in the y direction for small displacements (not a function of x or y), defined as:

$$P = \varepsilon_o \frac{V^2}{2g^2} t$$

where t is the cantilever thickness, V is the applied DC voltage between the electrode and cantilever, ε_o is the permittivity of free space, and g is the actuation gap of the cantilever. I is the moment of inertia of a cantilever defined as:

$$I = \frac{1}{12}tw^3$$

with t as the cantilever thickness. Integrating equation 3.1, we obtain:

$$d(x) = \frac{P}{24EI}x^4 + C_1x^3 + C_2x^2 + C_3x + C_4$$
 2.8

with C_1 , C_2 , C_3 , C_4 all constants. Due to clamped end conditions $C_3 = C_4 = 0$, since d(0) = d'(0) = 0 for this case. The set of equations pertaining to the free end of the cantilever are similar d''(L) = d'''(L) = 0. Differentiating Equation 3.4 two and three times respectively and using x = L, gives the system of equations:

$$d''(L) = \frac{P}{2EI}L^2 + 6C_1L + C_22 = 0$$
2.9

$$d'''(L) = \frac{P}{EI}L + 6C_1 = 0$$
 2.10

which can be solved for both C_1 and C_2 :

$$C_1 = -\frac{P}{6EI}L$$

$$C_2 = \frac{P}{AEI}L^2$$

this result can then be used to express the displacement versus x of the cantilever:

$$d(x) = \frac{P}{2EI} \left(\frac{x^4}{12} - \frac{Lx^3}{3} + \frac{L^2x^2}{2} \right)$$
 2.13

The maximum displacement of the cantilever is the relevant design parameter, calculated by evaluating the value of w(x) at x = L, which will give the maximum displacement of the beam:

$$d(L) = \frac{PL^4}{8EI}$$

Plugging in P and I as in Equations 3.2 and 3.3, we come to the final result for maximum displacement:

$$d_{\text{max}} = \frac{3\varepsilon_o V^2 L^4}{4g^2 w^3}$$
 2.15

Using this expression (Equation 3.11) to calculate maximum amplitudes for a variety of widths and lengths of the cantilevers produces curves such as Figure 2.2.3. After a displacement larger than the width of the cantilever, the above assumptions no longer hold, however these calculations were performed to estimate the smallest displacements of a cantilever with a given geometry which are well within these limits.

Displacement versus length (1 μm 0V gap, 26V actuation voltage)

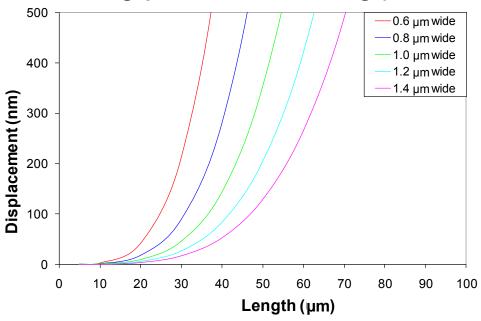


Figure 2.2.3 Plot of maximum displacement versus length of cantilever for a variety of cantilever widths, with a cantilever thickness of 2 μm.

In addition to the amplitude, pull-in voltages are calculated for the same lengths and widths of cantilevers. Pull-in is defined as the point at which the electrostatic force applied to the cantilever overcomes the spring restoring force. This causes instability, closing the gap between electrode and cantilever. Pull-in can cause permanent stiction, a destructive process with these devices.

The pull-in voltages are calculated using the model developed by [82] which accounts for cantilever bending, fringing field effects, and a number of other third order effects that change the cantilever pull-in voltage. This method is used to determine appropriate actuation gaps and feasible dimensions for the cantilevers. The simulation is performed for a range of widths, lengths, and actuation gaps. These calculations give an approximate maximum voltage before pull-in will occur. Figure

2.2.4 illustrates the pull in voltages versus the lengths of the cantilevers for two actuation gaps and a number of cantilever widths.

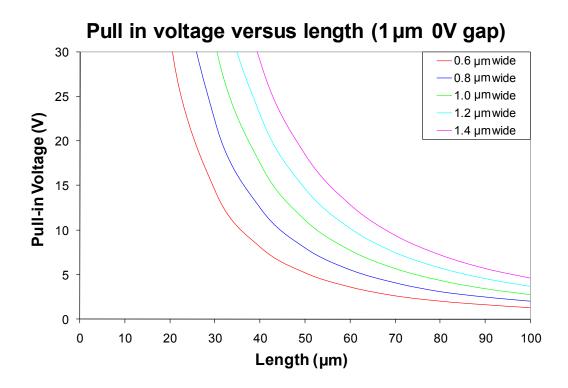


Figure 2.2.4 Pull in voltage versus length for two different actuation gap widths.

2.2.2 Optical Coupling Modeling

Optical overlap integrals were calculated assuming free space Gaussian beam propagation in the axial (z) waveguide direction [83]. A diagram in Figure 2.2.5 shows relevant parameters for this derivation.

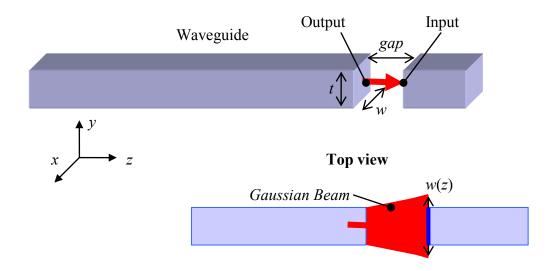


Figure 2.2.5 Diagram showing relevant dimensions and features for Gaussian beam propagation calculations.

The Gaussian beam equation of intensity as a function of x or y is shown in:

$$I(x, y, z) = \frac{2}{w(z)t(z)\pi} e^{\frac{-2y^2}{t(z)^2}} e^{\frac{-2x^2}{w(z)^2}}$$
2.16

With w(z) and t(z) the beam widths as a function of propagation distance:

$$w(z) = w \left[1 + \left(\frac{\lambda z}{\pi w^2} \right)^2 \right]$$
 2.17

$$t(z) = t \left[1 + \left(\frac{\lambda z}{\pi t^2} \right)^2 \right]$$
 2.18

With w and t the widths and thicknesses respectively. The mode overlap from the output facet to the input facet, T, is given by the following [83]:

$$T = \left| \iint I_{output}(x, y, gap) I_{input}(x, y, gap) dx dy \right|^2$$
 2.19

where z has been replaced with the gap length to simulate the propagation over this distance. From previous tests and projection lithography experience, the smallest

consistently resolvable feature size with available equipment has been found to be 0.6 μm , therefore all calculations use 0.6 μm gap lengths.

Considering the photodetector used, an estimate of about 5% optical coupling change is the lower threshold for observing waveguide movement through the optical coupling loss. For the $0.6~\mu m$ wide cantilever scenario, this corresponds to approximately 200 nm of misalignment (see Figure 2.2.6).

Due to this limitation, devices below 20 μ m long would not be measurable. Regardless of this 200 nm "limit," actuation at the resonant frequency can be as large as the quality factor (Q) times the DC static displacement, which for most devices the Q was estimated to be between 10-100, citing previous results [84]. For this reason, a number of devices were designed to operate at below the DC 200 nm "limit" to investigate the operation at these very short lengths (10 – 15 μ m long).

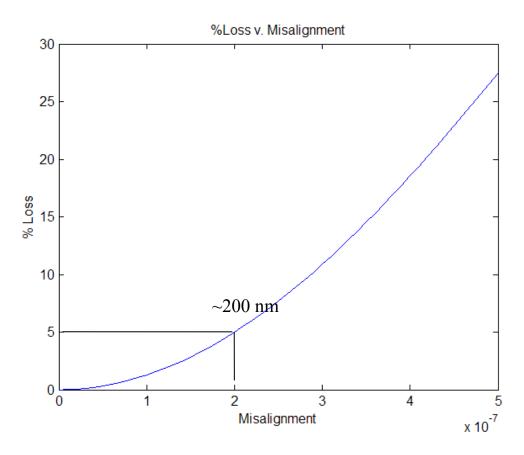


Figure 2.2.6 Percentage optical coupling loss versus cantilever misalignment (in meters). Superimposed is the 5% limitation, showing intersection at approximately 200 nm.

2.2.3 Cantilever Geometries

These calculations and design considerations were meant to better understand the potential capabilities of the sensor system. Final cantilever designs spanned a frequency range of 31.8 kHz to 5.3 MHz with cantilevers at 0.6 μ m wide, 100 μ m long and 1.0 μ m wide, 10 μ m long, respectively for those frequencies. The range of theoretical sensitivities as defined in Equation 2.4 for this range of devices are 2.754×10^{13} and 2.754×10^{16} Hz/g respectively. An abbreviated device listing is presented in Table 2.1, with a full presentation in Appendix A.

Table 2.1 Sample of cantilever geometries and calculated design parameters.

Length (µm)	Width (µm)	Actuation Gap (µm)	Resonant frequency (KHz)	Actuation (nm) @ max (26V)	Estimated Pull in voltage
10.0	0.6	0.6	3179.79 7.21		62.40
50.0	0.6	1.0	127.19	27.19 1622.88	
100.0	0.6	2.0	31.80	6491.54	3.40
10.0	0.8	0.6	4239.72	3.04	96.07
55.0	0.8	1.0	140.16	1002.40	6.61
100.0	0.8	2.0	42.40	2738.62	5.24
10.0	1.0	0.6	5299.65	1.56	134.26
45.0	1.0	2.0	261.71	57.50	36.17
100.0	1.0	1.0	53.00	5608.69	2.79
15.0	1.2	0.6	2826.48	4.56	78.44
50.0	1.2	2.0	254.38	50.72	38.51
100.0	1.2	2.0	63.60	811.44	9.63
15.0	1.4	0.6	3297.56	2.87	98.84
50.0	1.4	1.0	296.78	127.75	18.51
100.0	1.4	1.0	74.20	2043.98	4.63

2.2.4 Layer Structure Design

The layer structure, shown in Figure 2.2.7, which is used in the fabrication of our cantilever waveguides is a generic structure carried over from previous iterations of this device [84], and has no active regions. A starting semi-insulating (Fe doped) InP substrate is used in Molecular Beam Epitaxy (MBE) to grow each layer. An In_{0.53}Ga_{0.47}As layer is grown lattice matched to InP to provide a single crystal layer which can be selectively etched from InP using a proper wet etch which is described in the following chapter. A thin layer of alternating p-type and n-type In_{0.99}Ga_{0.01}As_{0.01}P_{0.99} regions are then grown to act as reverse biased P-N junctions which serve to prevent leakage currents during electrostatic actuation. Beyond these junctions the In_{0.99}Ga_{0.01}As_{0.01}P_{0.99} waveguiding layer is grown, again lattice matched with the layer beneath. This single crystal waveguiding layer is doped n-type at 1×10¹⁵ cm⁻³ to facilitate electrostatic actuation. The doping level is kept low enough

to prevent excessive waveguide losses due to free carrier absorption. A highly doped capping layer is used for achieving ohmic metal contacts.

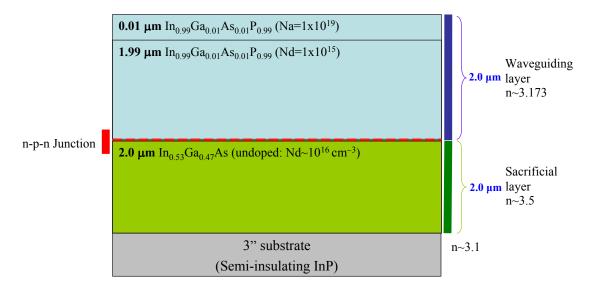


Figure 2.2.7 Diagram of layer structure for cantilever waveguide resonators

2.2.5 Cantilever Mask Design

Fabrication of InP cantilever waveguides (no active optoelectronic devices) is an established process requiring 2 masks to complete [15, 23, 85]. A mask which defines the waveguides and cantilevers is first designed. Care is taken to isolate contact pads to prevent the actuation of multiple devices at once. While waveguides as narrow as 0.6 µm are used in this design, all input and output waveguide facets are designed to be 2.5 µm wide to decrease the effect of mode mismatch from the spot size of the tapered optical fibers used in the test setup (Chapter 5). These wider regions are adiabatically tapered to the desired waveguide size over a 1 mm length. This increases the coupling into our devices and relaxes the tapered optical fiber alignment requirements. Design of the cantilevers and waveguide dimensions will be further discussed in a later section in this chapter.

Structures are placed on the mask which will serve to act as "release indicators" for the sacrificial release step. These are comprised of a number of bars with varying widths and lengths that are not anchored to any larger area that would not be removed by the sacrificial etch. During the sacrificial release step in the fabrication these bars will be monitored to estimate the lateral etch progression and to determine when the release has reached completion.

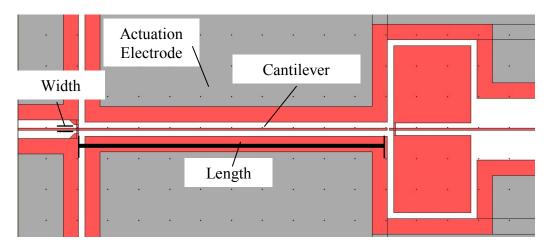


Figure 2.2.8 0.6 μm cantilever mask layout. Grey areas are metal and red are waveguide definitions.

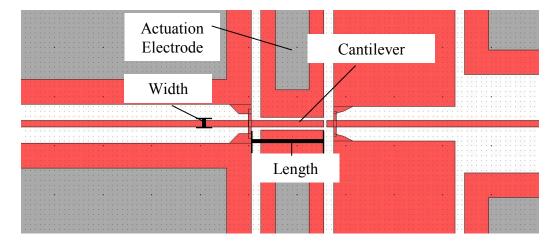


Figure 2.2.9 1.4 µm cantilever mask layout. Grey areas are metal and red are waveguide definitions.

A second mask is designed which defines the metal contact pads to achieve electrical connectivity. These pads are placed directly over the intended electrodes

and bias pads defined in the first mask with slightly reduced dimensions to give leeway for any misalignment during this successive exposure.

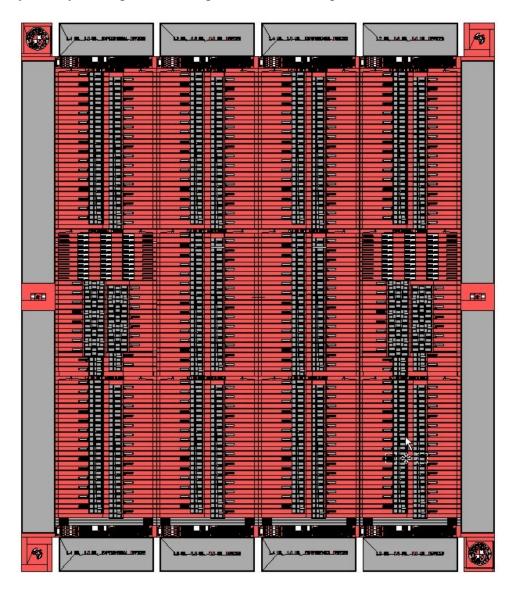


Figure 2.2.10 Full die image of cantilever waveguide devices red is unetched InP, Grey is metal deposition.

2.3 Waveguide Integrated PIN Photodetector Design

Design of the integrated optical detector follows closely with that of the well-studied waveguide PIN photodiode. The primary purpose of the waveguide PIN

photodiode is to reduce the response time of the photodiodes by decreasing the transit time of generated photocarriers.

2.3.1 Photodetector Modeling

Looking closer at the layer structure used for passive cantilever waveguides (shown in Figure 2.2.7) it is clear that a waveguide photodiode can be realized with minimal modifications. While the high speed is not a necessity for this application, the device geometry directly lends itself to using one of these waveguide integrated photodiode structures as a photodetector in the InP platform.

The absorption from the waveguide into the absorbing layer is dependent on the thicknesses of these layers and their relative indices of refraction. This is seen by observing modes from the waveguide region coupling into the modes of the absorbing layer. It is therefore expected that there is an ideal thickness of the absorbing layer for the particular wavelength being used (1550 nm). This is indeed the case, as shown by Emeis *et al* [74] where they present a theoretical calculation illustrating this behavior for a very similar structure as in the cantilever waveguides discussed earlier (see Figure 2.3.1).

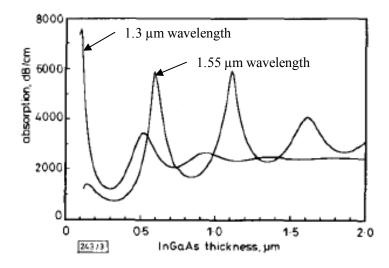


Figure 2.3.1 Numerical calculations of absorption versus absorbing layer thickness adapted from [74] for two radiation wavelengths in an InP/InGaAs/InP PIN photodiode.

For the design presented here, a finite element (FE) simulation was performed for the proposed layer structure to calculate an ideal thickness of the InGaAs absorbing layer. The COMSOL Multi-physics electromagnetic wave propagation module was used to simulate the waveguide propagation of 1550 nm light through a region containing the underlying InGaAs layer. A two dimensional model was constructed with the assumption that the width is much larger than the thickness of the absorbing and waveguide regions. Additionally, the length and width of the absorbing region were not considered, as their relationship to the absorption was deemed to be relatively simple and negligible respectively, in comparison to the absorbing layer thickness.

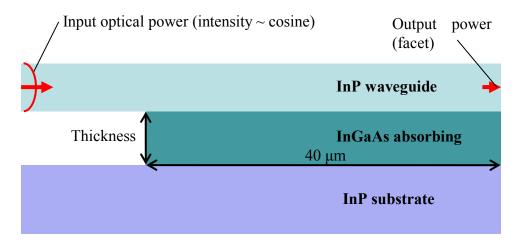


Figure 2.3.2 Diagram of simulation schematic with relevant items labeled.

A cross sectional portion of the absorbing region, schematically shown in Figure 2.3.2 was modeled. The input optical power was introduced as shown in the schematic with intensity as a cosine shape to simulate the first mode in the waveguide. Simulations are carried out for a range of thicknesses of the absorbing

region. Measurements of the power not absorbed within the length of the absorbing region are made by integrating over the output waveguide facet and measuring the total optical power at this point. Additionally, the "resistive heating" term is measured in the entire absorbing region to estimate the efficiency of the absorbing layer at various thicknesses. In the COMSOL Multi-physics software package, all absorption mechanisms are represented with this resistive heating term, assuming a lossy dielectric model. The resulting simulations produced very similar, periodic results to [74] which are shown in Figure 2.3.3. An example of two simulations at a maximum and minimum in absorption are shown in Figure 2.3.4.

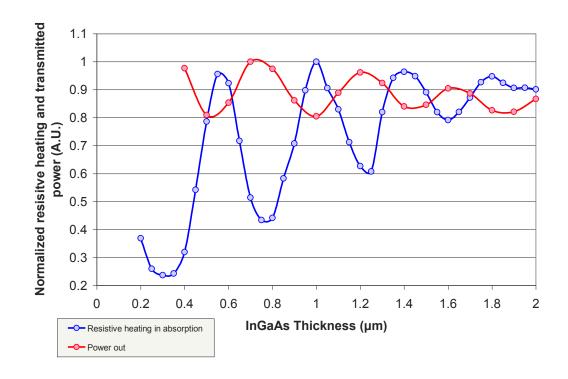


Figure 2.3.3 Simulation results showing resistive heating and transmitted optical power versus InGaAs thickness.

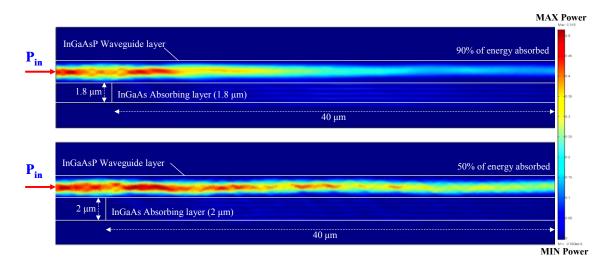


Figure 2.3.4 Two simulation results showing optical power density in two different designs, 1.8 μm absorbing layer and 2.0 μm absorbing layer.

From Figure 2.3.3, it is clear that there are a number of points at which maximum absorption occurs. The absorbing InGaAs layer will also serve as a

sacrificial layer; therefore mechanical issues also need to be taken into account while choosing a final layer thickness. A release layer that is very thin will be more prone to experience stiction than a thicker release layer, and its undercut rate will be affected with a change in thickness. A final decision was made to use $1.8~\mu m$ thick absorbing layer to maintain a similar fabrication process to that which was used previously ($2.0~\mu m$), and still maintain a high absorbance in the photodetector regions. This thickness is also more tolerant to any errors in thickness made during the epitaxial growth process.

2.3.2 Photodetector Layer Structure Design

Adjusting the layer structure involved the changing of the substrate from a semi-insulating substrate to a conductive n-type substrate to facilitate the N contact for the PIN photodiode. N-type substrates were chosen due to their ready availability since p-type doping does not considerably affect the optical properties of the waveguides. The p-n junction previously used to prevent leakage are removed in the modified layer structure to complete the PIN layer structure and allow the conduction between layers. Doping of the waveguide layer is moderate to reduce any free-carrier absorption within the waveguides, with the exception of a highly doped capping layer for ohmic contacts. The absorbing and sacrificial layer of In_{0.53}Ga_{0.47}As is grown undoped. This is important to create a large depletion region between the N and P contacts and create an absorption region where recombination is low, providing the photocurrent. The revised layer structure is shown in Figure 2.3.5.

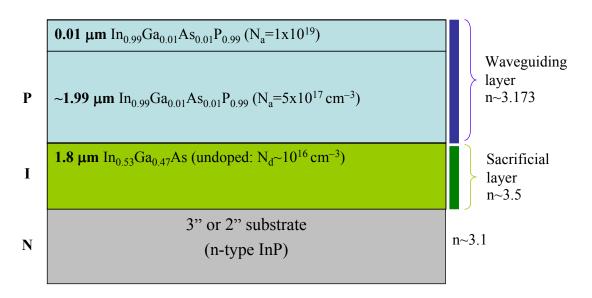


Figure 2.3.5 Revised layer structure for the integrated photodetectors.

2.3.3 Photodetector Mask Design

The design of the photodetectors is based upon the controlled undercutting of the sacrificial and absorbing InGaAs layer. To create regions which act as photodetectors, portions of waveguides will be made wide enough to prevent them from being fully underetched during the cantilever release. These will be the photodetector regions after the process is complete because they maintain the InGaAs underlayer. The mask used to achieve this is shown in Figure 2.3.6.

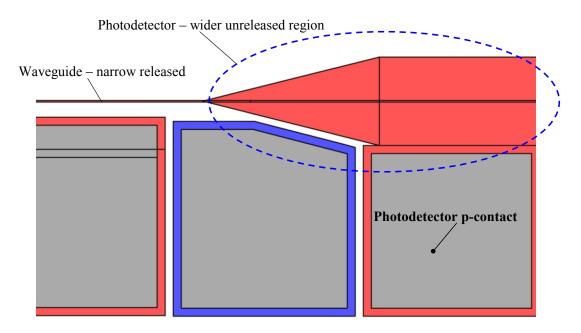


Figure 2.3.6 Mask design of detector regions. Under the same undercut etch, the photodetector region will remain, while the thin waveguide region will be released completely.

While design was undertaken for the thickness of the absorbing layer, the width of the detector regions was not simulated due to the high complexity of a 3 dimensional problem. Instead, a number of detector widths and lengths were designed to be tested to study the effect of the changing geometries.

The RC response of these photodetector regions is also a concern. The simple parallel plate capacitance and ohmic resistance is used to estimate the time constant for this simplified system, using τ =RC. After performing these calculations to find the RC time constant, it is clear that the cutoff frequency of the photodiodes is on the order of 1.9 GHz, which is well beyond the range of any resonant frequencies that will be encountered.

Devices for this new layer structure will consist of two major subsets: waveguides terminated by photodetectors of varying sizes and cantilever waveguides terminated with photodetectors, again with the same varying sizes. These devices are

meant for the characterization of the photodetector response and establishing whether the assumption that size of the absorbing region has little effect on the overall performance of the detector is valid. They will also allow for different biasing schemes to be implemented. Cantilevers with integrated photodetectors are meant to test the premise of the entire cantilever waveguide sensor platform.

2.3.4 Photodetector Geometries

Waveguide widths of 0.6, 1.2, 2 μ m will be used for the static detector-only designs with detector widths of 12 to 55 μ m, and lengths of 10-100 μ m. Waveguide widths were chosen to span the available waveguide widths used in previous generations. The detector widths and lengths were bounded by what would be the smallest size (12 μ m) due to the InGaAs undercut etch which will undercut 3 μ m in all directions. This parameter is based upon releasing the largest waveguide width on the chip (2.5 μ m), and the standard procedure of overetching about 50% to assure complete waveguide release.

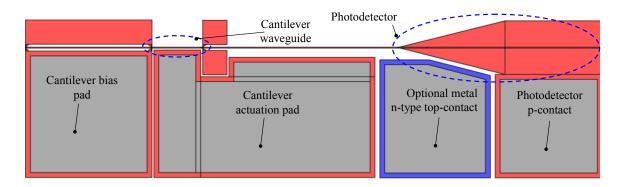


Figure 2.3.7 Mask image of cantilever integrated with waveguide with components labeled.

Cantilever waveguides integrated with the in-line photodetectors are chosen to represent a conservative range of device sizes. This was done to maximize the usability of the devices fabricated. Waveguide widths of 1.4 and 1.0 μ m, and lengths of 30, 50, and 100 μ m were used for the cantilever waveguides. Detector widths and lengths were also varied for these devices, from 25 to 55 μ m wide and 25 to 100 μ m long. An abbreviated listing of devices with photodetectors is listed in Table 2.2 and Table 2.3, while a complete listing is given in Appendix B.

Table 2.2 Photodetectors with straight waveguides. All values are present for 3 wavegide widths.

Waveguide widths (μm) :	0.6, 1.2, 2		
Width (µm)	Length (µm)		
12	10		
12	100		
25	25		
25	100		
40	25		
40	100		
55	25		
55	100		

Table 2.3 Photodetectors integrated with cantilevers.

Det	ector	Cantilever					
Width (µm)	Length (µm)	Actuation gap (μm)	Length (µm)	Width (µm)	f _o (KHz)		
25	25	2	100	1	53		
25	50	2	50	1	211.99		
25	75	2	30	1	588.85		
25	100	2	100	1.4	74.20		
25	25	2	50	1.4	296.78		
25	50	1	30	1.4	824.39		
40	25	2	100	1	53		
40	50	2	50	1	211.99		
40	75	2	30	1	588.85		
40	100	2	100	1.4	74.20		
40	25	2	50	1.4	296.78		
40	50	1	30	1.4	824.39		
55	75	2	50	1	211.99		
55	75	2	30	1	588.85		
55	100	2	100	1.4	74.20		
55	75	2	50	1.4	296.78		
55	100	1	30	1.4	824.39		

A noted difference in these designs is the single actuation electrode, in comparison with the previous configuration where the device could be actuated from either side. In this iteration, the single actuation was chosen to save space on the mask. These cantilever devices were also designed with metal pads at the tips of the cantilevers. This was done for future mass measurements where thiols could be eventually tethered to and used as a functionalization layer. This metal pad was placed on half of the cantilever devices. A full die image of the mask is shown in Figure 2.3.8.

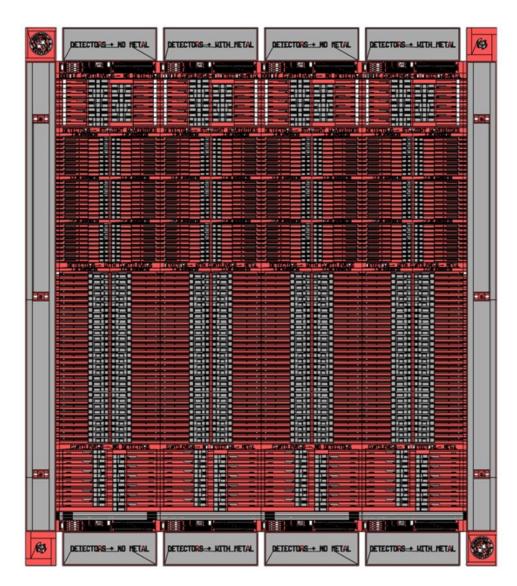


Figure 2.3.8 Full die image of integrated photodetector devices mask.

3 Fabrication

All MBE wafer growths are carried out at the Laboratory for Physical Science (LPS) by S. Kanakaraju with the specified parameters in the previous chapter. All fabrication with exception of the critical point drying is performed at the LPS class 10 cleanroom facility.

3.1 Cantilever Waveguide Fabrication

Starting with a 3 inch MBE wafer (615 μ m thick) with the layer structure as described previously (Figure 2.2.7), the wafer is partitioned into 16mm×17mm chips. A 7000 Å silicon dioxide hard mask is deposited on a 15×15 mm chip by high density plasma enhanced chemical vapor deposition (HDPECVD, Oxford Plasmalab model System 100) with deposition parameters: 5 minutes 140 W RF with NH₃ flow rate of 20 sccm as an adhesion promoter, and 21 minutes at 4W RF, and 500W on the inductively coupled plasma (ICP) coil with flow rates of N₂O and SiH₄ at 20 and 4 sccm respectively. This oxide layer is patterned with a 1 μ m thick resist (Fujifilm OIR-906-10) exposed on a 5× projection lithography system. The transfer of the photoresist pattern to the oxide is performed using CHF₃/O₂ plasma at 100W RF with a flow rate of 10 sccm CHF₃ and 3 sccm O₂ (Plasmatherm RIE model 790).

A cyclic methane-hydrogen RIE etch is used to etch the InGaAsP and InGaAs layers 3-5 µm deep [86-88]. An extensive chamber conditioning step is performed without a sample before any etching takes place. This step is necessary to prevent micromasking and grass formation [87]. The etch process switches between a methane and hydrogen etching cycle which etches the InP and InGaAs layers and

leaves a residual polymer which covers the sample surface as the etch progresses. A directional O₂ plasma is then used to remove the polymer from the bottom of the etch, leaving polymer to protect the sidewalls of the etch during the successive etch cycles. A 30 minute chamber conditioning step is performed between every 3 etching cycles to reduce the formation of grass and micromasking. The etching parameters are as follows: etch at 440 W DC bias with flow rates for H₂ and CH₄ at 32 and 8 sccm respectively, clean with a plasma at 200W DC and 10 sccm of O₂. The chamber condition step consisted of a 90 minute O₂ plasma chamber clean (200W RF power with 19 sccm of O₂), and a 30-60 minute etch procedure as explained above. Using this cyclic process, etches can achieve better than 85° sidewall angle. A SEM in Figure 3.1.1 shows the resulting scalloped sidewalls due to this type of etching; surface roughness is better than 30 nm.

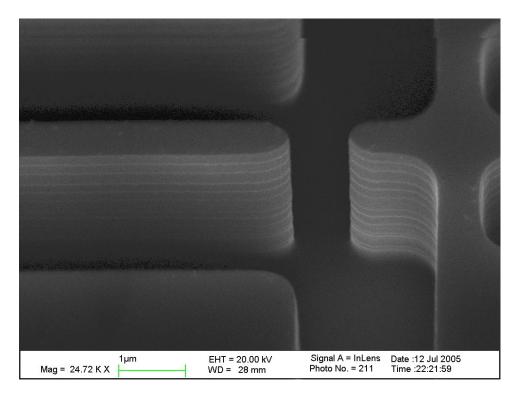


Figure 3.1.1 SEM of an InP etch showing "scalloped" sidewall due to the cyclic etching process.

A negative resist (Futurrex NR7-1500 PY, 1.5 μm thick) is used to pattern openings for the metal contacts using the same lithography system. Metal consisting of Ni-Au-Ge-Ni-Au (50Å–800Å–400Å–300Å–2000Å) deposited using electron beam evaporation (model CHA Industries Mark 40) on the photoresist. This metal is a commonly used ohmic contact in the LPS fabrication facility for III-V n-type compounds [87]. Ni acts as an adhesion layer, Ge-Au form a eutectic alloy, Ni acts as a barrier layer, and Au acts as an anti-corrosion metal pad [89]. A final patterning, by liftoff, is performed by removing the underlying photoresist with acetone overnight [87]. The final ohmic contact is made with a rapid thermal anneal (model Heatpulse 610) at 400 °C for 40 seconds in an N₂-H₂ ambient.

Optical quality waveguide facets are required to allow the input and output of light. This is achieved by cleaving along the crystal planes, achieving very smooth facets. To assure better device cleaving, the chip is thinned to 150-200 µm using a mechanical polishing wheel (Logitech model PM2A) with a 9 µm aluminum oxide slurry. A laser scribe is used to create defects that divide the chip into 4 slivers which contain devices. It is then cleaved along these scribed lines. A crossectional image of a cleaved surface is shown in Figure 3.1.2 where levels of the layer structure are apparent.

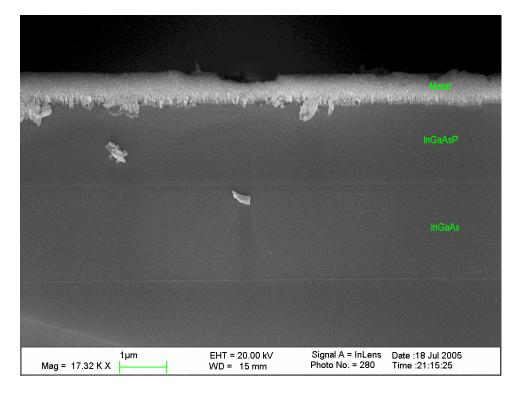


Figure 3.1.2 SEM of profile after a cleave has been carried out. The layer structure is visible in this image.

The release of the cantilever devices is then performed in a HF:H₂O₂:H₂O (1:1:8) solution which etches the sacrificial InGaAs layer nearly 100% selectively from the waveguide layer at a lateral etch rate of approximately 500 nm per minute. Release bars on the chip of varying widths and lengths are used to monitor the progress of the underetch. A completely released bar indicates a complete removal of the InGaAs layer beneath, and thus can help gauge the degree of cantilever release. Throughout this process, the sample is never removed from solution and dried to prevent surface tension forces from causing stiction of cantilevers and suspended waveguides against the substrate and sidewalls.

The fabrication process is completed by using a critical point dryer (Tousimis Samdri®-795) to prevent stiction from occurring. A CO₂ critical point dryer takes liquid CO₂ through its critical point into a gaseous state, avoiding surface tension

forces which can cause destruction of free-standing structures. Once dried, the chips are mounted on aluminum sample holders which allow for safe handling of the thin and delicate InP chips. SEM's of released structures are shown in Figure 3.1.3, Figure 3.1.4, and Figure 3.1.5.

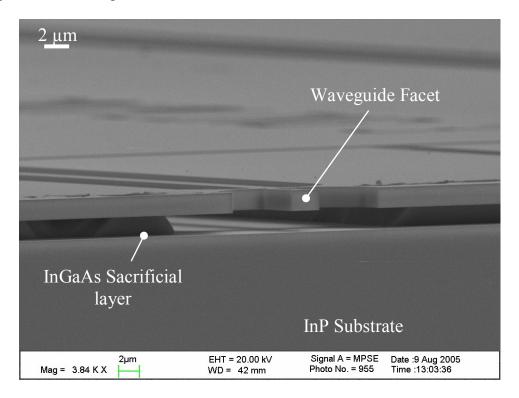


Figure 3.1.3 Image of waveguide facet after critical point drying, showing complete release and undercut of InGaAs.

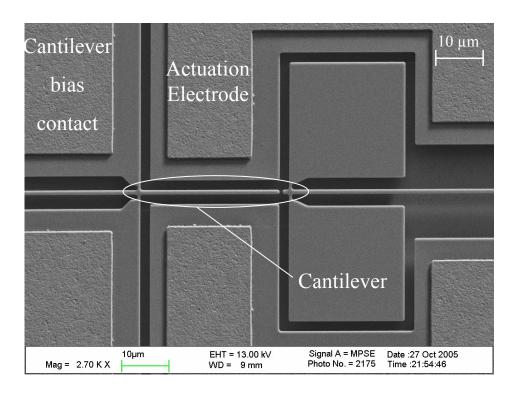


Figure 3.1.4 SEM of 1.0 μm wide, 30 μm long suspended cantilever resonator.

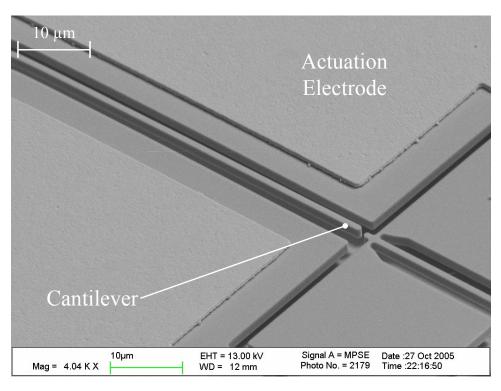


Figure 3.1.5 SEM of released cantilever, 75 μm long 1 μm wide.

3.2 Photodetector Fabrication Modifications

Some of the basic fabrication processes were modified to facilitate the changes in doping types (metal layers), the structural changes (conductive substrate), and InGaAs etching chemistries when making integrated PIN photodiodes. This section presents some of the major changes in the fabrication process flow.

3.2.1 Metal layers

As the doping type of the waveguides changed from n-type to p-type, this top layer no longer required the same metal alloy to provide for ohmic contacts. Instead, the top metal pads were replaced with another metal layer structure, Ti-Pt-Au (50 Å - 800 Å - 2000 Å). This serves as a good ohmic contact to p-type InP [90]. In this case the Ti acts as an adhesion layer, Pt a barrier layer, and Au as a top contact.

3.2.2 Backside Contacts

For this PIN configuration, a contact to the substrate must be made. To make any good contact with the backside of the substrate after the coarse thinning processes (9 µm alumina slurry), a second polishing step using 1 µm alumina slurry needed to be carried out to achieve a mirror finish, providing a better surface for the backside metal contacts. N-type contacts were deposited using the same metal layer structure as described previously (Ni-Au-Ge-Ni-Au), and annealed in the same manner. In the case that this method did not provide sufficient electrical contact for device performance, the top metal layer was modified to provide a contact window to the substrate from the top side of the wafer, indicated in Figure 2.3.7. In practice, this was never needed as the backside contact proved to be more than sufficient.

3.2.3 Release Etch

The release etch performed in previous device fabrication used hydrofluoric acid (HF) as a primary component, which aggressively etches titanium, the adhesion layer for the new top metal contacts. Regardless of the thickness, using HF in the etch delaminated all of the metal pads by removing this layer beneath, as can be seen in Figure 3.2.1.

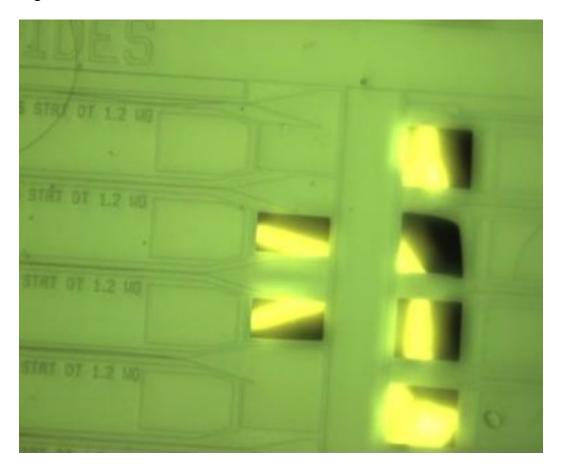


Figure 3.2.1 Optical microscope image of metal pads delaminating after immersion in HF containing solution.

Other etching chemistries exist for the selective removal of InGaAs with selectivity to InP [91, 92]. Replacing HF with other acids will also function the same way, with varying selectivities between InP and InGaAs. One such acid which is less

reactive with the metals involved in all of the metal contacts is H_3PO_4 [92]. This acid was mixed in the same ratios with H_2O_2 and H_2O as previously performed, a solution of H_3PO_4 : H_2O_2 : H_2O (1:1:8).

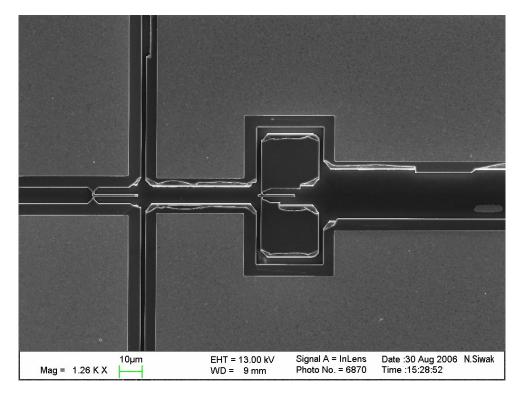


Figure 3.2.2 SEM image of destroyed cantilever.

This solution did not attack any of the metal contacts, but did create gas bubbles during the undercutting process. Voids created by the bubbles prevent the complete etching of the sacrificial layer and makes it difficult to gauge etch rates and the degree of release.

Ultrasonic agitation was attempted to break up bubble formation; however, the surface tension of the generated bubbles in combination with the high energy of the ultrasonic agitation was sufficient to destroy a large number of devices as can be seen in Figure 3.2.2. Reduction in the energy of agitation, achieved by gently tapping the solution beaker manually, proved to be the most reliable method to eliminate

bubble formation. Images of fabricated devices after the CO₂ critical point drying can be seen in Figure 3.2.3.

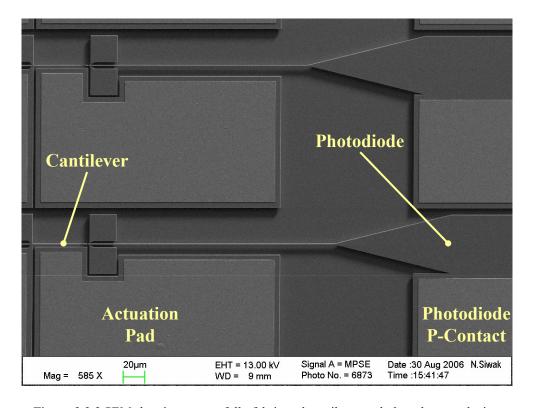


Figure 3.2.3 SEM showing successfully fabricated cantilever and photodetector devices.

3.3 Pentacene Morphology Characterization

In collaboration with projects here at the University of Maryland, and in an attempt to begin the development of a chemical sensor utilizing an active absorption layer as a transduction method, an organic semiconducting material, Pentacene (Pn), was chosen. This material is used often in organic transistor fabrication due to its high hole mobility. It has been shown in literature to volumetrically absorb gasses in the bulk phase of Pn crystal. This study explored the absorbing properties of thin film Pn crystals in the context of an cantilever coating. This layer has the added advantage of being compatible with the current fabrication process and pre-fabricated devices.

Surveying literature showed that Pn had never been reported as deposited on a InP surface. Papers did show how deposition parameters affected the film morphology, as well as possible interactions with the underlying substrate. The deposition of Pn on an InP surface is carried out to understand any complications which might arise due to the specific crystal properties.

3.3.1 Initial Film Deposition

All Pn depositions were performed at the LPS by Vince Ballarotto in an UHV vacuum sublimation deposition system. A shadow mask was employed to provide a method for measuring a step in the film to determine thickness. Depositions were performed on mechanical grade InP wafers as a first investigation of the deposition of Pn on this substrate. Samples included a patterned and etched sample, in addition to a planar unetched sample.

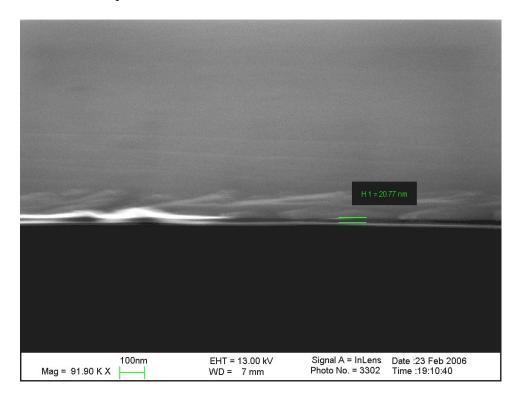
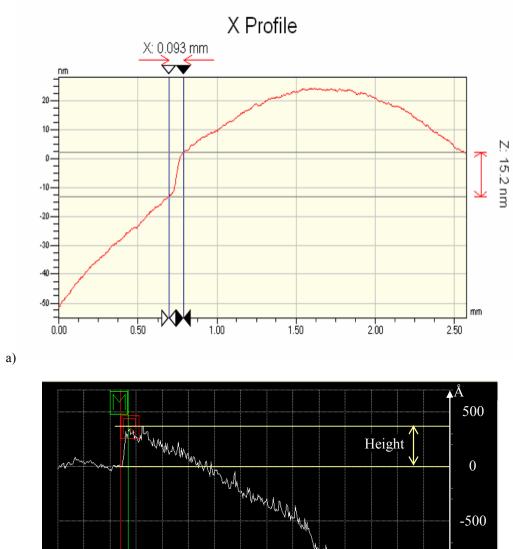


Figure 3.3.1 SEM profile image of substrate with deposited Pn with measured thickness

Measurements of the film thickness were performed by a number of methods. Crossections of deposited samples were measured using SEM (Figure 3.3.1), but due to limited resolution, other measurement methods were sought after to verify the deposition thickness. Next, measurements were performed with a contact profilometer, but these scans were damaging the surface due to the fragility of the Pn film and therefore resulted in an incorrect thickness. The subsequent deposition of a thin layer of gold in an atmospheric sputtering system (~50-100 Å) was able to provide the surface with sufficient reflectance to use the VEECO™ optical profilometer as shown in Figure 3.3.2a, and additionally gave the film enough stability to sustain scanning by the contact profilometer system, with scans shown in Figure 3.3.2b. Film thicknesses were verified to be in the range of 10-40 nm, as measured with the deposition setup using a crystal oscillator. Variations in thickness as observed for these Pn films are common at these thicknesses and result due to the layer formations in the bulk phase of growth [93-95].



b) Height 0
-500
-1000
-1500
-1500
-2000

Figure 3.3.2 a)VEECO optical profilometer scan of Pn deposition on InP created with a shadow mask, and **b)** contact profilometer scan of the same step.

Additionally, morphology of the film was as expected: exhibiting a nucleation phases, thin film phases, and a bulk phase [93, 95] at the edge of masked regions. Figure 3.3.3 illustrates clearly the three growth modes encountered during Pn deposition.

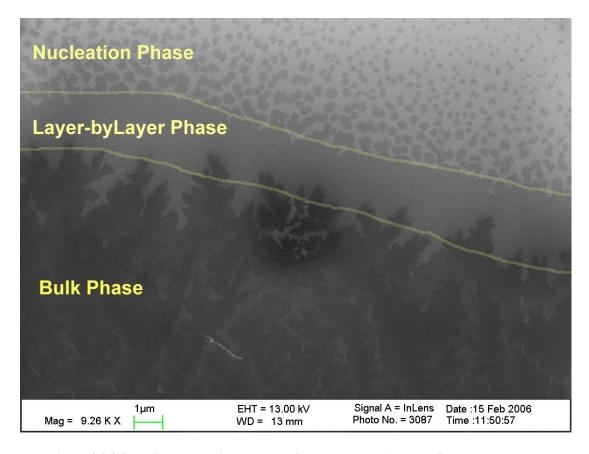


Figure 3.3.3 SEM image showing an edge of the masked region on a flat InP substrate.

Successful deposition of Pn onto planar and etched InP substrates validates any concerns of film morphology and structure due to crystal anisotropy. Sidewall deposition can be detrimental to the operation of the cantilever waveguides by closing and bridging the actuation gaps. This was investigated by depositing Pn with the same conditions on etched InP samples with similar patterns as would be encountered in real devices. Resulting tests showed no measurable sidewall coverage for features about 4 μ m deep with nearly 90 degree sidewalls. Actual devices have more shallow

heights of about $1.5-2~\mu m$ with slightly smaller (89 degree) sidewall angles. As would be expected with a UHV sublimation deposition process, the deposition was determined to be very directional, as no signs of deposition were observed on sidewalls in etched samples.

3.3.2 Deposition on Cantilever Devices

Once verification on test samples was completed, a chip with operational devices was introduced into the deposition chamber. While very little information about Pn absorption has been reported, literature indicates volumetric absorption into bulk Pn crystals [96] with a reversible effect. A thick layer of Pn was deposited, to allow for the largest possible volume for absorption of vapors and gases.

A 200 nm layer of Pn was chosen as the initial deposition thicknesses. This thickness is very large in comparison with normal Pn depositions (40-60 nm), but to measure significant absorption, a large volume is needed. For the device geometries of 1-2 µm used, the large thicknesses (10's of microns) used in [96] would not be acceptable for this application, while the typical thicknesses (50 nm) for electronic devices deposited at the LPS would provide insufficient volume. The 200 nm thickness was considered the thickest layer to be deposited using the available equipment at LPS and was also compatible with the micron-sized devices. Therefore, this thickness was used in this study.

Depositing such a thick film resulted in a coating which was likely predominantly bulk crystalline Pn, which forms after a number of single-crystal monolayers [93, 95].

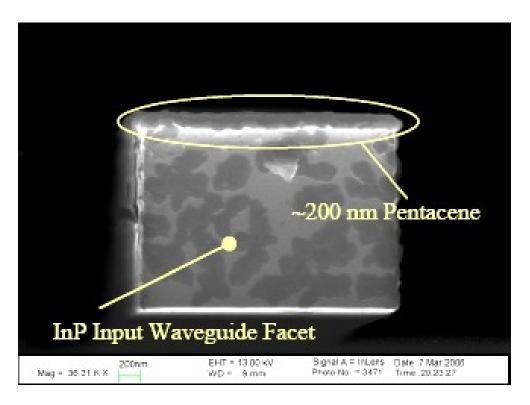


Figure 3.3.4 Input waveguide facet showing ~200 nm Pn deposition on the surface and nucleation on the facet.

Deposition on released cantilever devices did not affect the optical functionality of these devices despite the negligible accumulation on device sidewalls (see Figure 3.3.4 and Figure 3.3.5). Sidewall deposition was not directly measurable, amounting to nucleation or layer-by layer deposition phases, and thus was not greater than a few monolayers. Figure 3.3.4 shows the Pn layer deposited on the surface of a suspended waveguide facet, and also shows some of the sidewall deposition which is visible. Sidewall deposition was encountered due to a slight skew in the angle of the sample in the chamber, the slightly angled sidewalls, and the length of the deposition process. Another verification of the highly directional deposition can be seen in Figure 3.3.6 where a shadow masking effect can be seen as created by the suspended waveguides.

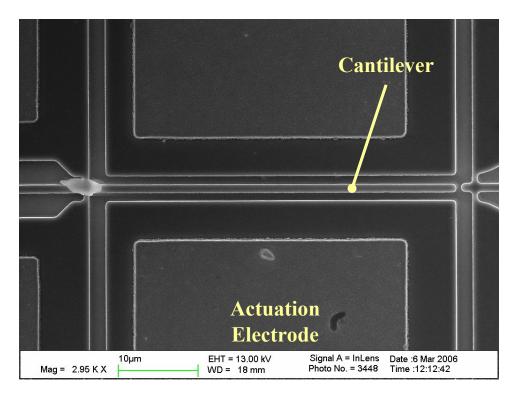


Figure 3.3.5 Top-down image of 45 μm long cantilever after Pn deposition, showing all features intact.

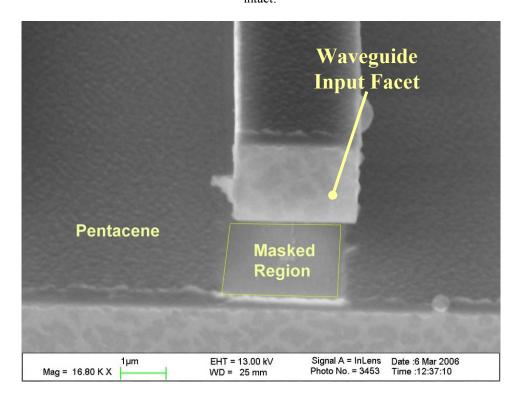


Figure 3.3.6 Input waveguide facet at an angle showing masking effect due to highly directional deposition.

Waveguide optical propagation was not eliminated as a result of the deposited material, although it was attenuated to varying degrees between devices. Significant loss was avoided primarily due to Pn's index of refraction being less than that of InP $(n_{InP} \approx 3.1, n_{Pn} \approx 1.56)$ [94]. Any losses which did occur can be attributed to scattering effects from sidewall roughness and the non-uniform Pn sidewall coverage.

In addition to inspection in SEM and optical propagation, electrical tests were performed to assure that isolated InP islands were not shorted due to the deposition of Pn. All testing results once again confirmed that the directional deposition had bridged no gaps between electrodes, and cantilever actuation remained unaffected.

A full test of the cantilever waveguides with optical propagation and electrical excitation was also successful, showing no effect but an expected resonant frequency shift due to the additional Pn mass on the cantilever. A bare 60 μ m long by 1.2 μ m wide cantilever was initially characterized having a resonant frequency of 231.3 KHz \pm 310 Hz. The same cantilever with Pn was measured with an average resonant frequency of 229.7 KHz \pm 153Hz. Using Equation 2.2 the 1.61 KHz frequency shift can be shown (see Figure 3.3.7) to correspond to a mass shift of 9.7×10^{-13} g. Based on the volume (60 μ m \times 1.2 μ m \times 0.2 μ m) of the Pn deposition on the top surface of the cantilever, the calculated Pn density is 0.674 g/cm³, less than 1.33 g/cm³ reported for bulk Pn [97]. The discrepancy in these values can be attributed to the uncertainty in Pn volume on the cantilever due to the varied height in Pn films. Bulk Pn crystals and thin films also do not have the same structure and

therefore cannot be assumed to have the same density, especially as any changes in deposition conditions affecting the film density significantly [95].

Without Pentacene With Pentacene Frequency (Hz) _ _

Without and With Pentacene Differentiation

Figure 3.3.7 Resonant frequency with and without pentacene

Measurement

4 Testing

4.1 Cantilever Waveguide Testing Setup

The testing setup to measure the cantilever resonators was a homemade system utilizing optical fibers, a long working distance microscope, micropositioners, a function generator, amplifier, and oscilloscope. A block diagram of the testing setup is shown in Figure 4.1.1. The core of the setup consists of parallel and opposing tapered single mode lensed fibers (Dow Corning SMF-28TM, 3.3 µm MFD, 0.020 mm to beam waist) which are mounted to an optical stage controlled by a series

of 3-axis electrostrictive micropositioners. The electrostrictive actuators are necessary for the fine adjustment needed to obtain maximum optical coupling into and out of our devices due to the small waveguide sizes. Between these lensed fibers is another optical stage which is moved in two axes using a manual micrometer drive screw. The devices are mounted for testing on this central stage. A large working distance microscope is used to assist in the placement of electrical probes, lensed fibers, and in verifying device operation via optical inspection.

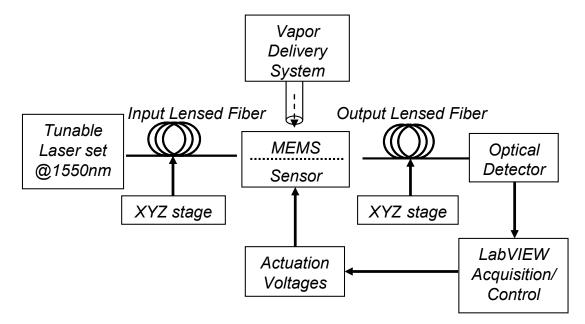


Figure 4.1.1 Testing setup block diagram.

Device testing was performed by coupling light at 1550 nm wavelength from a tunable laser source (New Focus VenturiTM Tunable Laser 1520-1620 nm) into the devices using a lensed fiber to focus the beam onto the waveguide input facet. A second lensed fiber collects light from the output waveguide facet which is then measured with a high speed photoreceiver (New Focus Model 1811 IR DC-125MHz Low noise photodetector). Both lensed fibers focus to a spot size of 3.5 μm and a focal length of about 20 μm. The analog photodetector output signal is captured with

an oscilloscope and then analyzed using MATLAB. Micropositioner probes are used to make electrical contact to the actuation electrodes to provide the in-plane actuation.

4.2 Testing Setup for Vapor Sensing

In order to perform vapor or gas sensing experiments, a number of modifications to the testing setup needed to be performed to isolate the cantilever waveguide resonators from the external environment and to introduce vapors. The core testing setup was not fundamentally changed; however additions were made to the setup described above.

4.2.1 Environmental Enclosure

A custom environmental enclosure was designed and built in-house. Components for manipulating the optical fibers and devices are contained in this environmental chamber made from Lexan (polycarbonate). This chamber is designed to isolate the system from external variables such as humidity variations or excessive dust. Included in the walls of the chamber are 2 optical feedthroughs, 16 BNC feedthroughs, 6 DIM feedthroughs for electrostrictive actuator control, and 4 Swagelok adapters. This allows electrical connections and optical connections to be made inside the chamber while closed, as well as tubes to be attached to introduce vapors. The lid is designed to be easily removed to allow the microscope to observe the devices under test, and then be replaced to further isolate the chamber. This provided a low-cost and effective solution for the first proof of concept tests. The inclusion of this chamber was deemed necessary after initial testing showed adverse effects from outside environmental variables during the simple resonator experiments.

4.2.2 Vapor Introduction

The introduction of vapor into the system to perform the sensing experiments is carried out through one of 4 Swagelok feedthrough adapters located on the environmental chamber. This method was used to test the effects of humidity on the sample by purging it with dry nitrogen. While effective, the equilibrium time constant of the chamber was shown to be long due to its large volume. This was directly encountered when performing the vapor sensing experiments. To address this problem, direct vapor introduction was chosen to prevent the lag in chamber condition which affects measurements.

Rather than relying on the environmental chamber to equilibrate to the desired conditions, the intended vapors were introduced at close proximity to the devices under test, more rapidly saturating the air being sampled by the sensors. This was performed using a small plastic capillary tube positioned by a micropositioner to serve as a nozzle. This nozzle was positioned to direct flow directly to the surface of the chip (see Figure 4.2.1), thereby removing equilibrium conditions existing with the entire chamber being filled.

This nozzle was fed by a flask containing a small amount of IPA or Ethanol (EtOH) allowed to evaporate at room temperature, shown in Figure 4.2.2. The vapor generated in the flask is delivered to the nozzle by way of a dry nitrogen stream as a carrier gas. The setup was further augmented by replacing the flask with a bubbler system, allowing for the gas stream to be saturated with vapor. Results presented here utilized this particular arrangement.

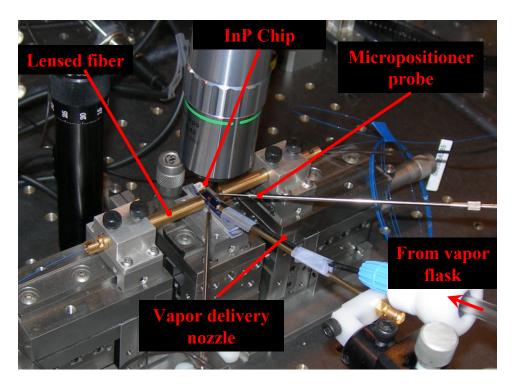


Figure 4.2.1 Photograph of device under test showing vapor delivery system.

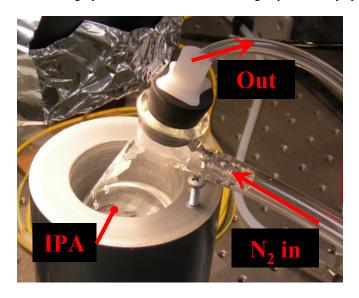


Figure 4.2.2 Flask containing liquid (IPA) to introduce vapors to device.

The testing procedure was as follows: Delivery nozzle was pointed directly to the top of the chip being tested, and the nozzle is used to direct dry nitrogen to the surface. Exposure time varied from 33 minutes to 1 hour in order to purge the Pn layer of any water or other vapors. The flask of alcohol was attached to the delivery

nozzle, and nitrogen is used to transport the vapor to the device surface for 33 minutes, until the resonant frequency stabilized at the shifted value. After exposure to the alcohols, the flask is removed and the device is again exposed to dry nitrogen to return it to the initial equilibrium state, for another 33 minutes. This process was repeated a number of times for both IPA and ethanol vapors. Throughout these steps, oscilloscope traces are captured using a LabView program every 2 to 10 seconds. Each oscilloscope trace contains the full ringing decay of the cantilever as measured through the high speed photodetector (see Figure 4.3.2).

4.3 Measurement Methods

4.3.1 Cantilever Waveguide Measurement

Two measurement schemes were implemented: a frequency sweeping (Figure 4.3.1), and a ringing technique (Figure 4.3.2). In a frequency sweep, frequency of the actuation signal is ramped while monitoring the amplitude of the output photodetector signal. As the frequency approaches the resonant frequency, the cantilever amplitude will increase to a maximum. This method of actuation and measurement is advantageous when measuring devices with high spring constants due to the increased cantilever response at resonance, but it is a lengthy process and therefore it used primarily as a verification of normal cantilever operation and any hidden resonances from outside influences. Cantilevers were measured using this method to establish the accuracy of theoretical predictions for resonant frequency. The highest resonant frequencies measured were accomplished using this measurement technique.

The ringing technique results from a square actuation pulse applied to the cantilever. The cantilever is pulled to the electrode and then released, allowing the dampened oscillations to be measured. This response contains the information of the resonant frequency of the cantilever, as well as any effects from dampening. This method of measurement is significantly faster than a frequency sweep, making it ideal for measuring the time dependence of resonant frequency in a sensing application. Stiffer cantilevers, however, do not experience significant displacement under allowed electrode volts (26V), thus limiting devices that can be read-out using this method.

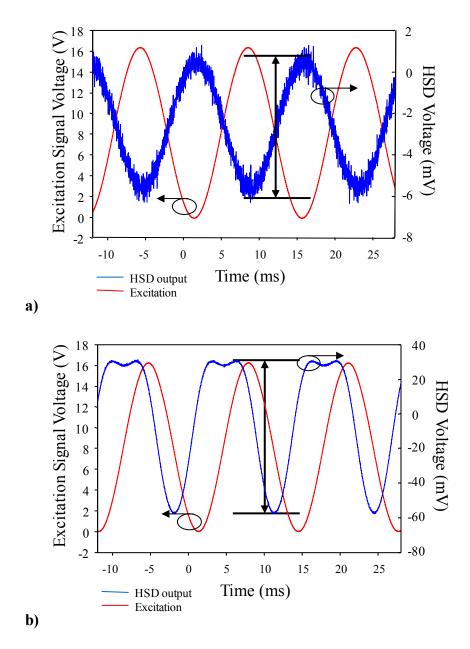


Figure 4.3.1 Illustration of how cantilever (dimensions 30 μm long, 1 μm width) response shown by high speed detector (HSD) voltage increases off and on resonance; **a)** off resonance, 700KHz, and **b)** on resonance, 758.8KHz.

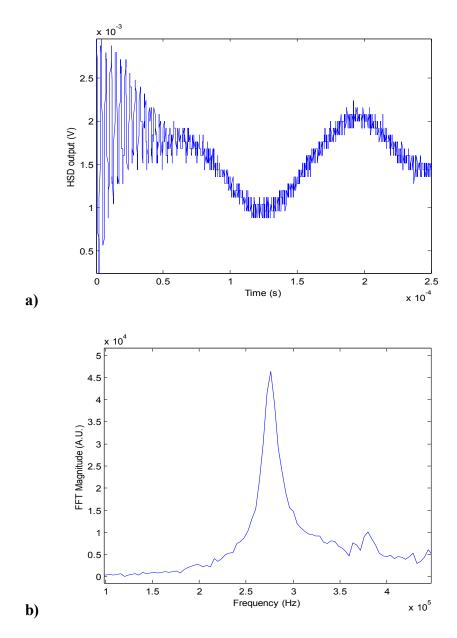


Figure 4.3.2 Ringing measurement of cantilever (dimensions 55 μ m long, 1 μ m wide). **a)** Raw ringing data and **b)** FFT of data.

4.3.2 Data Acquisition

Cantilever actuation is carried out by applying voltage signals generated from a function generator (Agilent 33220A 20 MHz function/arbitrary waveform generator) with approximately 10 V peak-to-peak amplitudes. Most devices are

actuated with less than 10 V, however for devices shorter than 30 µm, larger voltages are needed to actuate them appreciably. For this a 100V/V MEMS amplifier is used to amplify the output voltage from the function generator. The maximum voltage applied to the devices during testing was 40 V, 46% larger than the predicted value. This can be attributed to changes in layer structure from previous designs, and expected inconsistencies between growths. Higher voltages resulted in device failure due to dielectric breakdown through the InGaAs layer.

The output signal from the high speed photoreceiver is monitored with the oscilloscope, which is used to collect the temporal data representing cantilever movement. This data is transferred to a PC using a LabView program and via a GPIB interface. This application controls the frequency sweeping range and step size when performing a frequency sweep measurement. When performing a ringing measurement, the rate of sample acquisition is controlled with the program. This LabView control application is an essential tool to automate the data acquisition process, which is not practical using manual methods. An example of the LabView front panel program interface for the sweeping and the ringing measurements is shown in Figure 4.3.3and Figure 4.3.4, respectively.

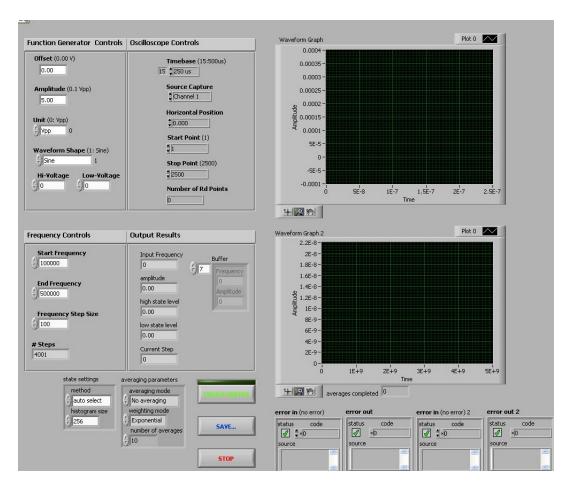


Figure 4.3.3 LabView interface for frequency sweeping program.

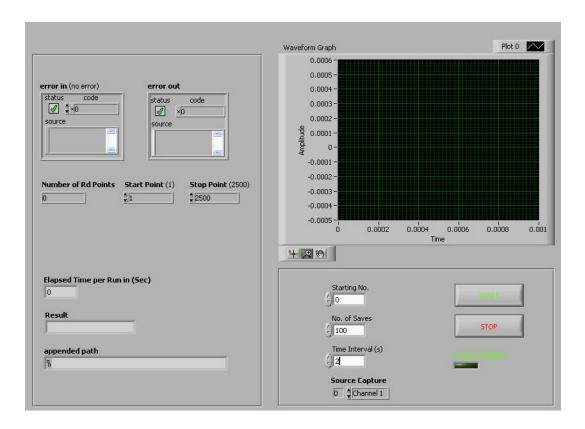


Figure 4.3.4 LabView interface for the ringing data save program.

4.3.3 Cantilever and Detector Biasing Schemes

The actuation of cantilevers using the substrate which enables PIN photodiodes proves to be more complicated due to the conductive path between the actuation and bias electrodes when any PIN junctions are forward biased. Care must be taken to assure that applied voltages keep the regions beneath each surface contact reverse biased at all times. The detector, actuation electrode, and cantilever bias electrode also each share a common terminal, the substrate contact, making the system susceptible to leakage currents. If these parasitic currents are large enough, they will overwhelm the optical signal from the photodiode. Figure 4.3.5 shows the scheme used to measure the photodetector current and apply actuation signals to the cantilever simultaneously.

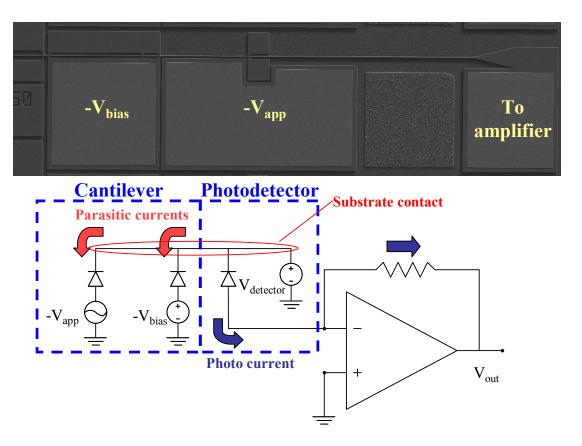


Figure 4.3.5 Photodiode measurement and simultaneous cantilever actuation schematic. Resistor in the transimpedance amplifier is set at $102 \text{ K}\Omega$.

By biasing the substrate at a positive voltage (1-2 V), the PIN diode is kept in a reverse bias configuration, and the transimpedance amplifier is isolated from any through-substrate parasitic currents generated from the actuation and bias voltages. Actuation and cantilever bias voltages are kept negative at all times to maintain the reverse bias at the PIN junction, and therefore set up a potential difference between the cantilever and actuation electrode, providing actuation of the cantilever beam.

4.4 Results

4.4.1 Cantilever Waveguides

Testing of the cantilevers with extended designs proceeded as described above. Measurements were performed using the frequency sweeping technique due to its greater versatility in measuring all devices geometries. Full characterization of these devices was carried out, with the measurements of the resonant frequencies and quality factors of the resonators. A final repeatability test was performed by taking a series of measurements (30-50) and taking their average and standard deviation to obtain a statistical estimate for the tested devices. A full listing of the measured and calculated values can be seen in Appendix C. This data represents the yield that was obtained after the fabrication. A number of devices were untestable due to structural damage; however, the devices which remained served to span the range of frequencies desired in this exploratory study. A selection of devices at the extremes of dimensions tested are listed in Table 4.1.

 Table 4.1 Selected testing results from cantilever waveguides.

Device			Fitted parameters	
Width (µm)	Length (µm)	Act. Gap (µm)	ω _o (KHz)	Q
1.2	100	1	82.60	8.92
1.2	45	1	410.34	56.38
0.8	10	0.6	5779.04	340.30
0.6	70	2	92.31	9.17
0.6	25	2	718.01	159.95

4.4.2 Cantilever Waveguide Vapor Sensing

After vapor sensing experiments were conducted and data processed, the resonant frequency was plotted versus time for each stage of the testing process. This dataset is used (a) to determine the resonant frequency shift, (b) calculate statistical parameters, and (c) to calculate an absorbed mass change. The raw data used in the following calculations are presented below. The fitted resonant frequency versus time, shown in Figure 4.4.1 for IPA vapors and Figure 4.4.2 for EtOH, shows two cycles of absorption and desorption for both vapors. An exponential decay function was fitted to the trend of the data, to estimate a time constant for absorption. In both cases, full recovery to the original baseline resonant frequency was obtained after purging with N₂.

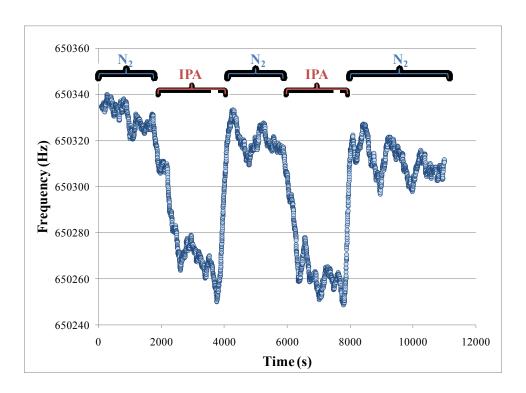


Figure 4.4.1 Plot of frequency versus time experienced during successive IPA introductions.

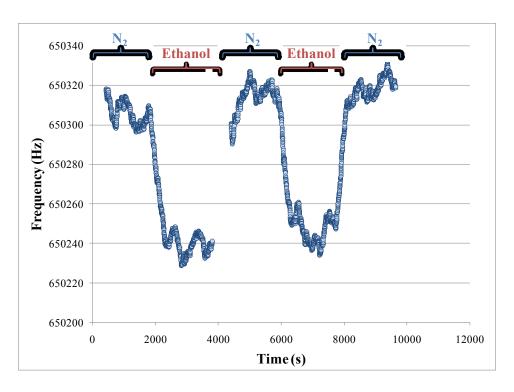


Figure 4.4.2 Plot of resonant frequency versus time during successive EtOH introductions

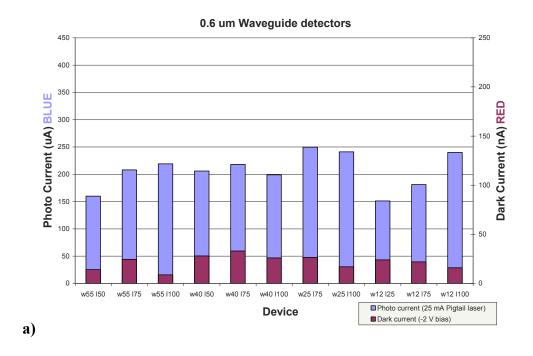
4.4.3 Integrated Photodetector Results

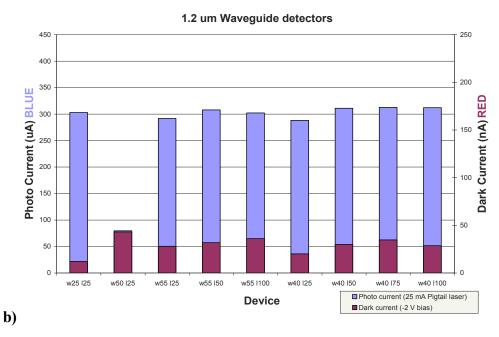
Testing of the integrated PIN photodiodes was carried out by first measuring the response of the static waveguide and photodiode devices to establish the expected dark current, and the effect of detector size on photocurrent. Once these baseline measurements were made, cantilever devices with the integrated photodiodes were tested. All devices were tested as described above, with only one input lensed fiber required due to the integrated PIN photodiodes replacing the output waveguides.

4.4.3.1 Static Photodetectors

Static detectors of various widths and lengths were tested for their photocurrent at a consistent laser power from a fiber pigtail laser with 25mA of forward current, and with the same lensed fibers for each device. Contact to the top metal pads is made using a micropositioner probe. The PIN photodiodes were biased

at -2 volts to maintain a reverse bias across the diode, and the current was measured using a picoammeter. Measurements of dark current (laser power off), and photo current (laser at 25mA forward bias) are made for each device. These results are presented below:





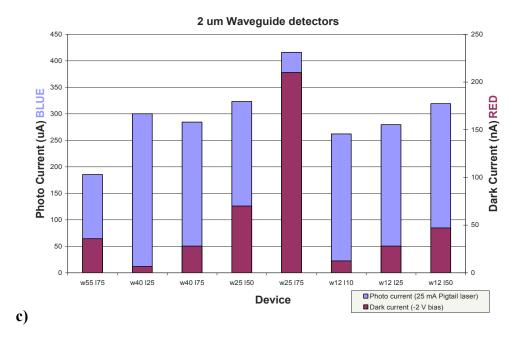


Figure 4.4.3 a), b), and c) Photo current and Dark current for the 3 waveguide widths and various detector sizes listed by their widths (w) and lengths (l). Each bar represents a different device described by its width (w) and length (l) in microns. Outlier data points in b) and c) are due to fabrication imperfections.

4.4.3.2 Cantilever Waveguides with Integrated PIN Photodetectors

Using the actuation scheme illustrated in Figure 4.3.5, all three cantilever lengths (30, 50, 100 μm) with integrated PIN photodetectors were tested using the same function generator as before with the ringing method for simple cantilever waveguide devices outlined above. Actuation of the 1 μm wide and 100 μm long cantilevers is measurable with an applied voltage of -8V peak-to-peak (see Figure 4.4.4). For the shorter cantilever devices, a 100V/V high-voltage amplifier was needed to achieve sufficient voltages (-30V peak-to-peak) to actuate the 50 μm long cantilever devices (see Figure 4.4.5). No measurable actuation was seen when attempting to actuate the 30 μm long cantilever devices. PIN junction breakdown

was measured to occur at over -50V of applied bias, after which point the actuation and bias electrodes become permanently shorted.

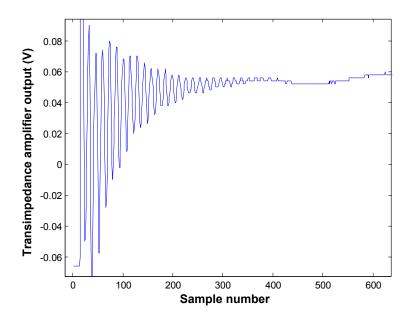


Figure 4.4.4 Underdamped response of 100 μm cantilever waveguide measured using the integrated PIN photodiode.

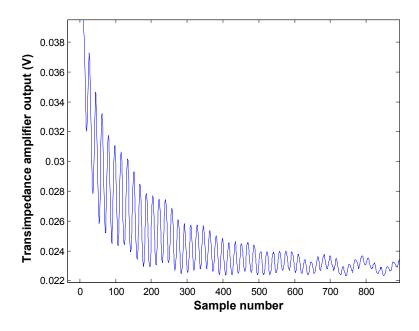


Figure 4.4.5 Underdamped response of 50 μm cantilever waveguide measured using the integrated PIN photodiode.

4.4.4 Summary

The results presented demonstrate the initial InP cantilever waveguide sensor to its practical limitations by investigating varying device dimensions and showing cantilevers with up to 5.8 MHz frequency operation. The extension of the sensing theory was applied to cantilever devices coated with an absorbing layer, Pn, which showed the validity of using the InP sensor system in a real-world application. These vapor sensing results verify the theoretical sensitivities calculated and reveal limitations in the measurement setup which affected the final sensitivity.

Integration of waveguide PIN photodiodes with the cantilever structures is also demonstrated for the first time. Testing of devices with varying photodetector dimensions provide a basis for minimum detector sizes, and shows that for this layer structure, very small photodetectors are sufficient for complete absorption of optical power. A biasing scheme is developed and shows through the results to be effective in actuating cantilever waveguide structures and providing bias voltage for the PIN photodiode simultaneously without excessive leakage current.

Each of these results will be analyzed and discussed in-depth in the proceeding chapters.

5 Data Analysis and Discussion

5.1 Resonant Frequency Analysis

For frequency sweeping measurements, the LabView program analyzes the amplitude of the output signal with respect to the actuation frequency and thus assembles the frequency spectrum in this way. For ringing measurements, the raw data is processed through a MATLAB program (Appendix D) which filters the data and takes the Fast Fourier Transform (FFT) of the set to obtain the frequency response.

The response actually obtained is due to the square wave actuation of the cantilever, a step response. This yields a frequency response that is not only the response of the cantilever but has a factor due to the excitation:

$$f(t) \xrightarrow{FT} F(j\omega) = H(j\omega)\hat{F}(j\omega)$$
 5.1

Where F(t) is the original function measured with the photodetector, $H(j\omega)$ is the frequency response of the cantilever, and $\hat{F}(j\omega)$ is the Fourier transform (FT) of the input excitation. Our input excitation, $\hat{F}(t)$, is defined as a step function with a well known Fourier transform, $\hat{F}(j\omega)$:

$$\hat{F}(j\omega) = \frac{1}{j\omega}$$
 5.2

Therefore Equation **6.1** becomes:

$$F(j\omega) = H(j\omega) \frac{1}{j\omega}$$
 5.3

To extract the real cantilever frequency response, we must divide the Fourier transform of the signal with the Fourier transform of the input, $\hat{F}(j\omega)$:

$$H(j\omega) = F(j\omega) \cdot j\omega$$
 5.4

Performing this operation allows us to extract the cantilever frequency response from the data collected, generally expressed with a Lorentzian function, shown in Equation **6.5**.

$$f_{lorentzian}(\omega) = y_o + \frac{A}{\pi w \cdot (1 + \left\lceil \frac{(\omega - \omega_o)}{w} \right\rceil^2)}$$
5.5

Where A is a normalizing parameter, w is the full-width-half-max, y_o is an offset, and ω_o is the resonant frequency. Additionally we define the quality factor, Q, as:

$$Q = \frac{\omega_o}{2w}$$
 5.6

A Lorentzian function is fitted to a subset of the data defined by a suitable frequency range which is chosen to include the entire resonant peak of the cantilever (established by visually inspecting the plot of the spectrum). The fitted parameters are then used to determine resonant frequency and quality factors as defined in Equations **6.5-6**. A MATLAB program was developed to automate this fitting task for an arbitrary number of data sets.

5.2 Frequency Shift Analysis

5.2.1 Exponential Fitting

As the precise mechanism of absorption is not known, an approximation is made by assuming that the transient absorption and desorption curves will tend towards an exponential behavior. An exponential function of the form:

$$f = y_o + e^{-x/b + a}$$
 5.7

is used to fit to the data points near the transient frequency shift point. The Mathematica mathematics software is used to perform the fitting operations and to display the results. Results of the exponential fits are tabulated in Table 5.1.

Table 5.1 Fitting results from exponential models

Equation: $f = y_o + e^{-x/b+a}$							
	Averaged Fitting parameters						
	IPA EtOH						
y_o	650243.60	y_o	650238.64				
а	4.23	а	4.61				
b	139.85	b	250.62				

The exponential decay function was fitted to the trend of the data, with an estimated time constant of the absorption of 5.3 minutes for IPA vapors and 4.2 minutes for ethanol vapor.

5.2.2 Calculated Mass Absorbed / Desorbed

Measurements of the difference of resonant frequency from the start to the end of each cycle are performed by averaging the steady state portions of the data as shown above. Table 5.2 shows the calculated frequency shift for the IPA and EtOH datasets, corresponding with Figure 4.4.1 and Figure 4.4.2. These resonant frequency

shifts are used in Equation 2.2 to solve for the absorbed mass. Dimensions of the cantilever were measured by SEM micrographs. Mass and moment of inertia of the cantilever are determined from the volume of the cantilever and the density of InP using familiar expressions for these values. Density of InP is found in the literature from [98]. Values for Young's modulus of our specific growths are found in [88]. The values of parameters and expressions in Equation 2.2 used for these calculations are listed in Table 5.3.

Table 5.2 shows the associated calculated mass shifts. In addition to these calculations, an estimate of the limitations of the testing setup using this device was found by equating the minimum Δf measurable from the standard deviation in measurement averages (~4.78 Hz). Using these values with Equation 2.2, a minimum Δm of 5.09×10^{-15} g is determined for this device and test setup.

Table 5.2 Calculated values for frequency and mass shifts as well as uncertainties on these values

IPA	EtOH			
Frequency shift (Hz)				
-61.57	-68.46			
Mass s	shift (g)			
6.56×10 ⁻¹⁴	7.28×10 ⁻¹⁴			
Frequency shift	uncertainty (Hz)			
11.0	10.5			
Mass change uncertainty (g)				
1.17×10 ⁻¹⁴	1.12×10 ⁻¹⁴			

Table 5.3 Parameters and expressions used to calculate absorbed/desorbed mass

Parameter	Value / Expression
E	80 GPa
I	$\frac{w^3t}{12}$
m_o	$l \cdot w \cdot t \cdot \rho_{inp}$
c_o	0.24
c_A	0.24
$ ho_{inp}$	4810 kg/m^3
l	60 μm
w	1 μm
t	1.71 μm

5.3 Discussion

5.3.1 Cantilever Resonators

Due to the high dampening conditions when operating in ambient environments, the quality factors of most resonators were below 100; an expected result for these cantilevers [53, 99]. The quality factor increases with the resonant frequency due to reduced dampening losses experienced by the smaller displacements of high frequency resonators [99]. The first MHz resonators using InP cantilever waveguides were demonstrated with smaller device geometries. The highest sensitivity measured with these devices was made using a 0.8 μ m wide, 10 μ m long cantilever. This device exhibited a resonant frequency of 5.78 MHz, with a quality factor of 340. The calculated sensitivity of this device is 4.4×10^{16} Hz/g.

The tested cantilevers illustrate their flexibility and the potential for high sensitivity using these devices in a detection system. While state-of-the-art mass microbalances achieve sensitivities of approximately 2×10^{19} Hz/g (a resolved mass of 6.3 attograms, 10^{-18} g) [33], several orders of magnitude greater than the measurements demonstrated here, these ultra high sensitivity results were measured

in a vacuum environment using a complex external optical setup. Using the platform developed here, one can achieve moderate sensitivities with a more compact and practical device.

5.3.2 Vapor Sensing

A drift was experienced over the data range which can be attributed to optical fiber misalignment due to electrostrictive actuator drift. This actuator movement did not affect the absolute frequency shift experienced by the resonators. Both the IPA and Ethanol caused statistically identical frequency shifts, which may be result of the molecule size compared to the available volume for absorption within the pentacene layer. Additionally, the time constants of the absorption of IPA and ethanol are not drastically different from one another. Response time seems to show a slight decrease with smaller molecules (EtOH), which may indicate the absorption mechanism is related to molecule size

The minimum Δm is believed to be largely limited by the current testing setup. Noise due to the external photodetector and possible transmission line effects due to external cabling is a factor in the measurements, reducing the quality of the data fits and increasing the uncertainty between measurements. The majority of noise most likely arises due to changes in coupling of light onto and off chip using the lensed fibers. Ambient mechanical vibrations, actuator drift, and air currents all affect the placement of lensed fibers. As coupling is extremely sensitive to any displacement; the coupling into and out of the facets is affected by these external variables. The loss of signal even more dramatically reduces the quality of the data fits, creating larger spread in the resonant frequencies. Normal coupling strengths

vary from about 3 μ W to 0.300 μ W, which lies within the dynamic range offered by the photodetector. After the transmitted optical power drops to 100 nW, the resonator signal becomes nearly impossible to measure. This requires a constant human monitoring of the testing setup to keep a sufficient amount of optical coupling, which is not an efficient or very effective method to compensate for these issues, and thus introduces a large amount of uncertainty in the final data as a result of human error and reaction time.

In response to these issues, specifically the signal to noise ratio encountered in the devices, the introduction of additional integrated optical devices will improve this noise due to optical fiber misalignment. Chapter 4 will show the integration of photodetectors with the cantilever waveguides. This removes one of the optical fibers from the setup, reducing the effect of drift and vibration to only one actuator, making the drifting misalignment easier to compensate for. This change increases the stability of the data in comparison to the measurements shown above. Introducing baffles into the chamber to reduce the strength and directionality of air currents within the enclosure will assist in further reducing any optical fiber misalignment due to this stimulus. After these changes, if electrical noise is still apparent, more effort can be made to reduce the length of transmission lines between various connections.

Another challenge is the very small frequency shift measured with the pentacene thin film as an absorbing layer, indicating its low absorbance of these vapors tested. There are a number of factors which may have contributed to this effect. The large Pn layer thickness may be a reason for this discrepancy between absorption and desorption of differing vapors. It is also possible that a chemical

reaction between the alcohols and Pn such as oxidation of Pn to Pentacenequinone [96] may have contributed to the change in the absorption properties of the film during the first absorption measurements, making the two vapors indistinguishable. Ambient temperature differences between the absorption and desorption cycles will change relative rates of diffusion into and out of the Pn layer, and any temperature fluctuations which may have occurred contributed to this effect as the environmental chamber is not temperature stabilized.

5.3.3 Integrated PIN Photodiodes

5.3.3.1 Static Detectors

From the above measurements it is apparent that the assumption made during design of these PIN diodes was reasonable: that there is little or no trend observed in the difference between devices of various widths and lengths. For the waveguides of 0.6 and 1.2 μ m wide, the photocurrent varies little from device to device, indicating that optical power is completely absorbed in the detector region before it reaches the edges of the photodetector. An exception to this is in the narrowest detectors for 0.6 and 2.0 μ m wide waveguides which show a slight trend in increasing photocurrent with length. This could indicate a characteristic length required to absorb the optical power completely (\approx 4-5 μ m). In cases where the width of the detector is comparable to this characteristic value, detector length will play a bigger part in the total collected optical power.

For each of the devices, dark current is about 4 orders of magnitude less than the measured photocurrent for a moderate optical intensity. In most cases dark current stayed essentially constant (at approximately 25-50 nA) with changes in the

device geometries, with the exception of some of the larger waveguide detectors, where a slight increase can be seen which can be attributed to increased photodiode area. This trend is not conclusive since devices of approximately the same size do not show this increase, and in some cases show a decrease. Regardless of these inconsistencies, the dark current is sufficiently small (3 orders of magnitude) compared to the photocurrent. In lieu of this, these variations in the background dark current due to detector sizing can be ignored.

5.3.3.2 Cantilever Waveguides with Integrated PIN Photodiodes

It was observed that measurements of the cantilever waveguides with integrated photodiodes exhibited a peculiarity in the ringing measurements. underdamped oscillating response of the cantilevers was only measurable at the point of applied negative potential difference (the "upstroke"), rather than at the point of no applied potential (the "release") which would normally be used. Measurement using the upstroke of the step actuation is generally avoided because of frequency "tuning" based upon the applied voltage difference [15]. This arises from the energy that is stored within the capacitor made up of the cantilever and actuation electrode, effectively stiffening the cantilever with higher applied voltages. The effect is clearly seen in the 50 µm long cantilever device tested (see figure Figure 5.3.1). If actuation maintains a consistent voltage, the resonant frequencies measured should likewise remain consistent for the set of measurements with the same device. The fact that no resonance was measured at the release cycle indicates an energy dissipation affect due to the high resistivity of the pathway between the cantilever and the actuation electrode which critically dampens these vibrations.

Resonant frequency versus applied voltage 305000 300000 Resonant Frequency Average 295000 290000 285000 280000 275000 270000 265000 260000 255000 -40 -30 -10 -50 -20 0 **Applied Voltage**

Figure 5.3.1 Illustration of frequency tuning effect. Resonant frequency versus applied actuation voltage.

Increasingly consistent measurements, a predicted effect of integrating PIN photodetectors on chip, were clearly seen in all devices tested. Deviations of resonant frequency between measurements for a 100 μ m cantilever ($f_o \approx 72$ KHz) were measured to be \pm 15 Hz, and for the 50 μ m long cantilevers ($f_o \approx 279$ KHz), \pm 35 Hz; which both exhibited dramatic improvement in measurement repeatability and stability over long datasets in comparison to the previous designs. The reduction in variability in the testing setup by the removal of one lensed fiber gives an explanation for this change. Not only does this integrated configuration produce more consistent measurements, but in the same respects it also simplifies the measurement procedures considerably by removing some random and human error associated with the previous experimental techniques.

The cantilever waveguides integrated with PIN photodetectors in general required larger actuation voltages than those measured previously with the passive cantilever waveguides. This can be attributed to a reduction in voltage drop because of leakage current through the InGaAs layer. Due to this effect, the required voltages for shortest cantilevers (30 μ m) exceeded the reverse PIN diode breakdown and thus were not useable. Additionally, a large amount of background leakage signal is measured due to capacitive coupling between the adjacent actuation and photodetector bias contacts. This background made obtaining measurements of damped oscillations difficult.

6 Conclusions and Future Work

6.1 Summary of Results Reported

This thesis presents the first stages in the development of an integrated cantilever waveguide resonator chemical sensor realized in InP. Extensions on first generation designs were aimed at exploring the limitations of this platform by achieving higher resonant frequencies and sensitivities. Cantilevers with resonant frequencies as high as 5.78 MHz, quality factors of 340 in air, and calculated sensitivities of $4.4 \times 10^{16} \, \mathrm{Hz/g}$ were demonstrated.

The first measurement of chemical vapors using the InP cantilever waveguide sensor system utilizing a Pentacene absorbing layer has also been demonstrated. The active absorption layer Pentacene was deposited on existing suspended InP devices for the first time and characterized. Isopropanol (IPA) and Ethanol (EtOH) vapors were introduced into an environmental chamber containing the cantilever waveguide resonators coated with the Pentacene absorbing layer. Mass shifts due to IPA and EtOH absorption of 6.56×10^{-14} and 7.28×10^{-14} g, respectively, have been measured for these devices with a minimum mass detection threshold of 5.09×10^{-15} g.

The design, fabrication, and testing of a PIN photodetector monolithically integrated with a cantilever waveguide resonator is reported. Optimal design of an epitaxial layer structure by way of numerical finite element modeling (FEM) simulations was carried out to determine the layer thickness for maximum absorption in the intrinsic region of a PIN photodetector. Fabrication modifications were made to the standard cantilever fabrication process flow to facilitate proper electrical

contacts and to determine compatible undercutting solutions to release the MEMS devices. Measurement of waveguide integrated PIN diodes was carried out for a variety of diode sizes, showing that diode sizes at a large scale do not affect maximum photocurrent significantly; dark currents for these detectors as low as 8.7 nA are demonstrated. The measurement of resonating cantilever waveguides was also carried out using the integrated waveguide photodiodes, showing an improvement in measurement repeatability, yielding frequency measurements with uncertainty of better than \pm 35 Hz, showing greater stability over time compared to the measurements of cantilevers with no integrated photodiodes.

6.2 Future Work

6.2.1 Layer Structure Modifications

The issues discussed in the measurement of the cantilever waveguides with PIN photodetectors may be addressed by modifying the future layer structures. A layer structure grown on a semi-insulating substrate with the n-doped side of the PIN diode as a grown layer rather than a n-type substrate (shown in Figure 6.2.1) will aid in isolating the actuation, biasing, and photodiode components from each other. Two separate etches will be performed: an initial etch to make contact with the n-type bottom layer, and an etch down to the substrate, electrically isolating the contact regions. This will prove to be especially crucial for the future designs of these devices with integrated optical sources which will require separate electrical excitation for each component, causing more pathways and possibilities for leakage currents.

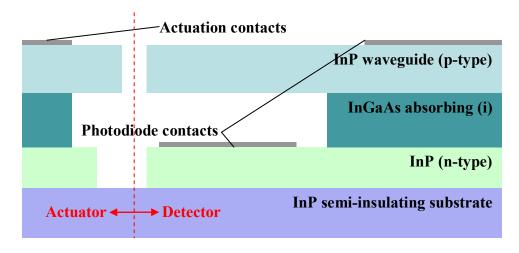


Figure 6.2.1 Illustration of how inserting an additional n-type layer into the epitaxial growth would isolate the detector and actuator regions electrically.

6.2.2 Functionalization and Absorbing Layers

This work presented the use of an active functionalization or absorbing layer Pentacene to measure the absorption of vapor onto the cantilever sensor. The fabrication of a solid-state chemical sensor within the context of this cantilever resonator needs to be investigated further. This will involve the optimization of Pentacene film growths to achieve high mobility semiconducting layers to be used in future organic thin film transistors (TFTs), as well as determination of the appropriate metal contacts for these organic TFTs. The combination of an organic TFT sensor and the cantilever mass sensor will provide additional selectivity in comparison to each device separately.

Apart from the development of an organic TFT on-chip, other absorbing layers should be investigated for future iterations of this cantilever sensor. Layers which have selective absorption to different analytes such as thiol groups would be ideal candidates for bringing greater selectivity to these cantilever sensors. Polymer materials, such as Poly(methyl methacrylate) (PMMA), Polyvinylalcohol (PVA), and

Polyethylene glycol (PEG) are only a small selection of available absorbing layers used for gas and vapor sensing [100]. These materials will be investigated to provide alternatives for absorbing layers and augment the existing studies using Pentacene. Investigating other absorbing layers with intent to use them simultaneously on multiple cantilevers will allow for principle component analysis to be performed. This provides a chemical "fingerprint" for any number of analytes, enhances the selectivity of the sensor, and even allows for compositions of differing analytes to be detected and measured.

6.2.3 Optical Source Integration

One of the stated benefits of using a III-V semiconductor as a device material is the ability for the optical readout to be monolithically integrated on-chip. The first component of this integrated scheme has been demonstrated in this thesis in the integration of a PIN photodetector with the passive cantilever waveguides. The logical progression would be to design an optical source for the system, providing a completely on-chip readout mechanism. A conceptual schematic of the final sensor system is shown in Figure 6.2.2.

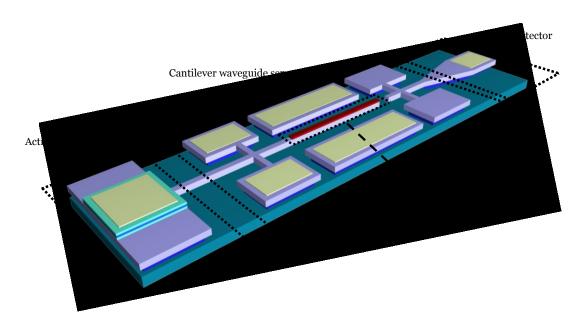


Figure 6.2.2 Schematic of fully integrated chemical sensor system in InP.

6.3 Conclusion

This work has demonstrated the first generation cantilever waveguide chemical sensor design and fabrication, with the inclusion of an active absorption layer, Pentacene, to measure the presence of IPA vapors. This presents the first time that Pentacene has been used as a volumetric absorbing layer for an InP cantilever waveguide vapor sensor. While the signal measured due to this absorption is not overwhelmingly large, it illustrates the capabilities of this sensor system. Future work investigating other absorption layers for use on these cantilever waveguides will further enhance the effectiveness and flexibility of these sensors.

The first integration of InP/InGaAs PIN photodetectors with these cantilever sensors has been successfully accomplished, providing increased measurement repeatability to the sensors and a simpler implementation of the optical readout. A new fabrication process has been established to fabricate cantilever waveguide resonators with PIN photodetectors. This study has also shown that careful biasing

and actuation is required for these devices to prevent detrimental leakage currents from obscuring resonance measurements. Lessons learned during these developments in both fabrication and testing will be directly applicable to future designs working with integrated optical sources.

Finally, the monolithic integration of these InP cantilever and PIN diode devices with active 1550 nm optical sources, and the exploration of using multiple absorptive materials, will facilitate novel, portable, and single-chip chem-bio sensors in the future.

Appendix A

	Length (µm)	Width (µm)	Actuation Gap (µm)	Resonant frequency (KHz)	Actuation (nm) @ max (26V)	Estimated Pull in voltage
	10.0	0.6	0.6	3179.79	7.21	62.40
	15.0	0.6	1.0	1413.24	13.15	57.69
	15.0	0.6	2.0	1413.24	3.29	151.29
	20.0	0.6	1.0	794.95	41.55	32.45
	20.0	0.6	2.0	794.95	10.39	85.10
	25.0	0.6	1.0	508.77	101.43	20.77
	25.0	0.6	2.0	508.77	25.36	54.46
40	30.0	0.6	1.0	353.31	210.33	14.42
) ers	30.0	0.6	2.0	353.31	52.58	37.82
0.6 µm wide Cantilevers	35.0	0.6	1.0	259.57	389.65	10.60
Ē	35.0	0.6	2.0	259.57	97.41	27.79
ä	40.0	0.6	1.0	198.74	664.73	8.11
O	40.0	0.6	2.0	198.74	166.18	21.28
<u>i</u>	45.0	0.6	1.0 157.03 1064.77	6.41		
>	45.0	0.6	2.0	157.03	266.19	16.81
틸	50.0	0.6	1.0	127.19	1622.88	5.19
9	50.0	0.6	2.0	127.19	405.72	13.62
0	55.0	0.6	1.0	105.12	2376.06	4.29
	55.0	0.6	2.0	105.12	594.02	11.25
	60.0	0.6	1.0	88.33	3365.21	3.61
	60.0	0.6	2.0	88.33	841.30	9.46
	65.0	0.6	1.0	75.26	4635.12	3.07
	65.0	0.6	2.0	75.26	1158.78	8.06
	70.0	0.6	1.0	64.89	6234.47	2.65
	70.0	0.6	2.0	64.89	1558.62	6.95
	75.0	0.6	1.0	56.53	8215.85	2.31
	75.0	0.6	2.0	56.53	2053.96	6.05
	100.0	0.6	1.0	31.80	25966.15	1.30
	100.0	0.6	2.0	31.80	6491.54	3.40

	Length (µm)	Width (µm)	Actuation Gap (µm)	Resonant frequency (KHz)	Actuation (nm) @ max (26V)	Estimated Pull in voltage
	10.0	0.8	0.6	4239.72	3.04	96.07
	15.0	0.8	0.6	1884.32	15.40	42.70
	20.0	0.8	1.0	1059.93	17.53	49.96
	25.0	0.8	1.0	678.35	42.79	31.97
	25.0	0.8	2.0	678.35	10.70	83.85
	30.0	0.8	1.0	471.08	88.73	22.20
	30.0	0.8	2.0	471.08	22.18	58.23
ပွ	35.0	0.8	1.0	346.10	164.39	16.31
\ e	35.0	0.8	2.0	346.10	41.10	42.78
<u>e</u>	40.0	0.8	1.0	264.98	280.43	12.49
ıı	40.0	0.8	2.0	264.98	70.11	32.76
µm wide Cantilevers	45.0	8.0	1.0	209.37	449.20	9.87
e G	45.0	0.8	2.0	2.0 209.37 112.30	112.30	25.88
ĕ	50.0	0.8	1.0	169.59	684.65	7.99
Ē	50.0	0.8	2.0	169.59	171.16	20.96
	55.0	0.8	1.0	140.16	1002.40	6.61
0.8	55.0	0.8	2.0	140.16 250.60		17.33
	60.0	0.8	1.0	117.77	1419.70	5.55
	60.0	0.8	2.0	117.77	354.92	14.56
	65.0	0.8	1.0	100.35	1955.44	4.73
	65.0	8.0	2.0	100.35	488.86	12.40
	70.0	8.0	1.0	86.52	2630.17	4.08
	70.0	0.8	2.0	86.52	657.54	10.70
	75.0	0.8	1.0	75.37	3466.06	3.55
	75.0	0.8	2.0	75.37	866.52	9.32
	85.0	0.8	1.0	58.68	5718.30	2.77
	100.0	0.8	1.0	42.40	10954.47	2.00
	100.0	0.8	2.0	42.40	2738.62	5.24

	Length (µm)	Width (µm)	Actuation Gap (µm)	Resonant frequency (KHz)	Actuation (nm) @ max (26V)	Estimated Pull in voltage
	10.0	1.0	0.6	5299.65	1.56	134.26
	15.0	1.0	0.6	2355.40	7.89	59.67
	20.0	1.0	1.0	1324.91	8.97	69.82
	20.0	1.0	2.0	1324.91	2.24	183.11
	25.0	1.0	1.0	847.94	21.91	44.69
	25.0	1.0	2.0	847.94	5.48	117.19
	30.0	1.0	1.0	588.85	45.43	31.03
ပွ	30.0	1.0	2.0	588.85	11.36	81.38
Cantilevers	35.0	1.0	1.0	432.62	84.17	22.80
<u>e</u>	35.0	1.0	2.0	432.62	21.04	59.79
ı	40.0	1.0	1.0	331.23	143.58	17.46
Sa	40.0	1.0	2.0	331.23	35.90	45.78
<u>8</u>	45.0	1.0	1.0	261.71	229.99	13.79
Ĭĕ	45.0	1.0	2.0 261.71 57.50	57.50	36.17	
µm wide	50.0	1.0	1.0	211.99	350.54	11.17
	50.0	1.0	2.0	211.99	87.64	29.30
1.0	55.0	1.0	1.0	175.19	513.23	9.23
`	55.0	1.0	2.0	175.19	128.31	24.21
	60.0	1.0	1.0	147.21	726.89	7.76
	60.0	1.0	2.0	147.21	181.72	20.35
	65.0	1.0	1.0	125.44	1001.19	6.61
	65.0	1.0	2.0	125.44	250.30	17.34
	70.0	1.0	1.0	108.16	1346.65	5.70
	70.0	1.0	2.0	108.16	336.66	14.95
	75.0	1.0	1.0	94.22	1774.62	4.97
	75.0	1.0	2.0	94.22	443.66	13.02
	100.0	1.0	1.0	53.00	5608.69	2.79
	100.0	1.0	2.0	53.00	1402.17	7.32

	Length (µm)	Width (µm)	Actuation Gap (µm)	Resonant frequency (KHz)	Actuation (nm) @ max (26V)	Estimated Pull in voltage
	15.0	1.2	0.6	2826.48	4.56	78.44
	15.0	1.2	1.0	2826.48	1.64	163.17
	20.0	1.2	0.6	1589.89	14.43	44.12
	20.0	1.2	1.0	1589.89	5.19	91.78
	20.0	1.2	2.0	1589.89	1.30	240.70
	25.0	1.2	0.6	1017.53	35.22	28.24
	25.0	1.2	1.0	1017.53	12.68	58.74
	25.0	1.2	2.0	1017.53	3.17	154.05
	30.0	1.2	0.6	706.62	73.03	19.61
ပွ	30.0	1.2	1.0	706.62	26.29	40.79
µm wide Cantilevers	30.0	1.2	2.0	706.62	6.57	106.98
<u> </u>	35.0	1.2	0.6	519.15	135.30	14.41
nt	35.0	1.2	1.0	519.15	48.71	29.97
Sa	35.0	1.2	2.0	519.15	12.18	78.60
<u>e</u>	40.0	1.2	1.0	397.47	83.09	22.95
Ni Ni	40.0	1.2	2.0	397.47	20.77	60.18
<u> </u>	45.0	1.2	1.0	314.05	133.10	18.13
<u> </u>	45.0	1.2	2.0	314.05	33.27	47.55
1.2	50.0	1.2	1.0	254.38	202.86	14.69
`	50.0	1.2	2.0	254.38	50.72	38.51
	55.0	1.2	1.0	210.23	297.01	12.14
	55.0	1.2	2.0	210.23	74.25	31.83
	60.0	1.2	1.0	176.65	420.65	10.20
	60.0	1.2	2.0	176.65	105.16	26.74
	65.0	1.2	1.0	150.52	579.39	8.69
	65.0	1.2	2.0	150.52	144.85	22.79
	70.0	1.2	1.0	129.79	779.31	7.49
	70.0	1.2	2.0	129.79	194.83	19.65
	75.0	1.2	1.0	113.06	1026.98	6.53
	75.0	1.2	2.0	113.06	256.75	17.12
	100.0	1.2	1.0	63.60	3245.77	3.67
	100.0	1.2	2.0	63.60	811.44	9.63

	Length (µm)	Width (µm)	Actuation Gap (µm)	Resonant frequency (KHz)	Actuation (nm) @ max (26V)	Estimated Pull in voltage
	15.0	1.4	0.6	3297.56	2.87	98.84
	15.0	1.4	1.0	3297.56	1.03	205.62
	20.0	1.4	0.6	1854.88	9.08	55.60
	20.0	1.4	1.0	1854.88	3.27	115.66
	25.0	1.4	0.6	1187.12	22.18	35.58
	25.0	1.4	1.0	1187.12	7.98	74.02
	25.0	1.4	2.0	1187.12	2.00	194.13
	30.0	1.4	0.6	824.39	45.99	24.71
	30.0	1.4	1.0	824.39	16.56	51.40
ပ္ပ	30.0	1.4	2.0	824.39	4.14	134.81
/er	35.0	1.4	0.6	605.67	85.20	18.15
<u>6</u>	35.0	1.4	1.0	605.67	30.67	37.77
nti	35.0	1.4	2.0	605.67	7.67	99.04
Ca	40.0	1.4	1.0	463.72	52.33	28.91
µm wide Cantilevers	40.0	1.4	2.0	463.72	13.08	75.83
ξi	45.0	1.4	1.0	366.40	83.82	22.85
<u> </u>	45.0	1.4	2.0	366.40	20.95	59.92
I⊒	50.0	1.4	1.0	296.78	127.75	18.51
4.1	50.0	1.4	2.0	296.78	31.94	48.53
`	55.0	1.4	1.0	245.27	187.04	15.29
	55.0	1.4	2.0	245.27	46.76	40.11
	60.0	1.4	1.0	206.10	264.90	12.85
	60.0	1.4	2.0	206.10	66.23	33.70
	65.0	1.4	1.0	175.61	364.86	10.95
	65.0	1.4	2.0	175.61	91.22	28.72
	70.0	1.4	1.0	151.42	490.76	9.44
	70.0	1.4	2.0	151.42	122.69	24.76
	75.0	1.4	1.0	131.90	646.73	8.22
	75.0	1.4	2.0	131.90	161.68	21.57
	85.0	1.4	1.0	102.69	1066.97	6.40
	100.0	1.4	1.0	74.20	2043.98	4.63
	100.0	1.4	2.0	74.20	511.00	12.13

Appendix B

Detectors - straight waveguides						
Waveguide width (µm) :	2					
~W (InGaAs after release)	Width (µm)	Length (µm)				
6.00	12	10				
6.00	12	25				
6.00	12	50				
6.00	12	75				
6.00	12	100				
19.00	25	25				
19.00	25	50				
19.00	25	75				
19.00	25	100				
34.00	40	25				
34.00	40	50				
34.00	40	75				
34.00	40	100				
49.00	55	25				
49.00	55	50				
49.00	55	75				
49.00	55	100				

Detectors - straight waveguides					
Waveguide width (µm) :	1.2				
~W (InGaAs after release)	Width (µm)	Length (µm)			
6.00	12	10			
6.00	12	25			
6.00	12	50			
6.00	12	75			
6.00	12	100			
19.00	25	25			
19.00	25	50			
19.00	25	75			
19.00	25	100			
34.00	40	25			
34.00	40	50			
34.00	40	75			
34.00	40	100			
49.00	55	25			
49.00	55	50			
49.00	55	75			
49.00	55	100			

Detectors - straight waveguides					
Waveguide width (µm) :	0.6				
~W (InGaAs after release)	Width (µm)	Length (µm)			
6.00	12	10			
6.00	12	25			
6.00	12	50			
6.00	12	75			
6.00	12	100			
19.00	25	25			
19.00	25	50			
19.00	25	75			
19.00	25	100			
34.00	40	25			
34.00	40	50			
34.00	40	75			
34.00	40	100			
49.00	55	25			
49.00	55	50			
49.00	55	75			
49.00	55	100			

Detectors - with cantilevers							
C	etector			Cantileve	r		
~W InGaAs (µm)	Width (µm)	Length (µm)	actuation gap (µm)	length (µm)	width (µm)	fo (KHz)	
19.00	25	25	2	100	1	53	
19.00	25	50	2	100	1	53	
19.00	25	75	2	100	1	53	
19.00	25	100	2	100	1	53	
19.00	25	25	2	50	1	211.99	
19.00	25	50	2	50	1	211.99	
19.00	25	75	2	50	1	211.99	
19.00	25	100	2	50	1	211.99	
19.00	25	25	2	30	1	588.85	
19.00	25	50	2	30	1	588.85	
19.00	25	75	2	30	1	588.85	
19.00	25	100	2	30	1	588.85	
19.00	25	25	2	100	1.4	74.20	
19.00	25	50	2	100	1.4	74.20	
19.00	25	75	2	100	1.4	74.20	
19.00	25	100	2	100	1.4	74.20	
19.00	25	25	2	50	1.4	296.78	
19.00	25	50	2	50	1.4	296.78	
19.00	25	75	2	50	1.4	296.78	
19.00	25	100	2	50	1.4	296.78	
19.00	25	25	1	30	1.4	824.39	
19.00	25	50	1	30	1.4	824.39	
19.00	25	75	1	30	1.4	824.39	
19.00	25	100	1	30	1.4	824.39	

Detectors - with cantilevers									
С	etector		Cantilever						
~W InGaAs (µm)	Width (µm)	Length (µm)	actuation gap (µm)	length (µm)	width (µm)	fo (KHz)			
34.00	40	25	2	100	1	53			
34.00	40	50	2	100	1	53			
34.00	40	75	2	100	1	53			
34.00	40	100	2	100	1	53			
34.00	40	25	2	50	1	211.99			
34.00	40	50	2	50	1	211.99			
34.00	40	75	2	50	1	211.99			
34.00	40	100	2	50	1	211.99			
34.00	40	25	2	30	1	588.85			
34.00	40	50	2	30	1	588.85			
34.00	40	75	2	30	1	588.85			
34.00	40	100	2	30	1	588.85			
34.00	40	25	2	100	1.4	74.20			
34.00	40	50	2	100	1.4	74.20			
34.00	40	75	2	100	1.4	74.20			
34.00	40	100	2	100	1.4	74.20			
34.00	40	25	2	50	1.4	296.78			
34.00	40	50	2	50	1.4	296.78			
34.00	40	75	2	50	1.4	296.78			
34.00	40	100	2	50	1.4	296.78			
34.00	40	25	1	30	1.4	824.39			
34.00	40	50	1	30	1.4	824.39			
34.00	40	75	1	30	1.4	824.39			
34.00	40	100	1	30	1.4	824.39			

Detectors - with cantilevers									
	etector		Cantilever						
~W InGaAs (µm)	Width (µm)	Length (µm)	actuation gap (µm)	length (µm)	width (µm)	fo (KHz)			
49.00	55	75	2	100	1	53			
49.00	55	100	2	100	1	53			
49.00	55	75	2	50	1	211.99			
49.00	55	100	2	50	1	211.99			
49.00	55	75	2	30	1	588.85			
49.00	55	100	2	30	1	588.85			
49.00	55	75	2	100	1.4	74.20			
49.00	55	100	2	100	1.4	74.20			
49.00	55	75	2	50	1.4	296.78			
49.00	55	100	2	50	1.4	296.78			
49.00	55	75	1	30	1.4	824.39			
49.00	55	100	1	30	1.4	824.39			

Appendix C

Data from cantilever waveguide resonators with fit parameters

parameters									
	Fitting function: $F_{lorentzian}(\omega) = y_o + \frac{A}{\pi w \cdot (1 + \left[\frac{(\omega - \omega_o)}{w}\right]^2)}$								
Device			Fitting parameters from MATLAB						
Width (µm)	Length (µm)	Act. Gap (μm)	A (Hz ²)	w (Hz)	ω _o (KHz)	y ₀ (A.U.)	$\begin{pmatrix} \mathbf{Q} \\ \frac{\omega_o}{2w} \end{pmatrix}$	\mathbb{R}^2	
0.6	25	2	0.0043	4488.98	718.01	-0.0001	159.95	0.9924	
0.6	30	2	0.0072	6429.86	511.44	0.0002	79.55	0.9959	
0.6	35	2	0.0121	8062.06	359.77	0.0008	44.91	0.9916	
0.6	45	2	0.0097	10511.95	217.03	0.0006	20.65	0.9959	
0.6	50	2	0.0027	6850.83	183.91	0.0001	26.85	0.9921	
0.6	70	2	0.0138	10285.11	92.31	0.0023	9.17	0.9981	
0.8	10	0.6	0.0030	16982.12	5779.04	0.0003	340.30	0.9520	
0.8	20	1	0.0081	10765.81	1367.09	0.0006	126.98	0.9818	
1.2	45	1	0.0142	8084.29	410.34	0.0015	56.38	0.9578	
1.2	50	1	0.1124	8583.68	334.28	0.0040	39.67	0.9921	
1.2	55	1	0.0006	5679.31	383.08	0.0001	67.55	0.9404	
1.2	60	1	0.0065	9464.15	229.02	0.0007	24.35	0.9945	
1.2	65	1	0.0078	7516.38	196.30	0.0006	26.20	0.9869	
1.2	75	1	0.1274	6884.49	147.27	0.0103	21.41	0.9951	
1.2	100	1	0.0377	10066.93	82.60	0.0029	8.92	0.9912	

Appendix D

```
function null=multiplefft(filenamestart, savename, start, stop)
%filenamestart: name of the first file (assuming sequential numbering)
%savename: place to save all the data from the fits
%start: starting filename number
%stop: stopping filename number
Getfft arguments
%getfftcsv(filename, savename, mode)
%fitlorentzianmultiple arguments and returns
%[x0 Q w y0 R]=fitlorentzianmultiple(filename, range, mode)
%This program will take the starting file in a directory and then incrament the file
%name and use the getdata function to get all of my FFTs
%Also will plot the last fft dataset so i can get the range
%then i fit all the data, and save the different aspects of the fits
if start<10
   num=int2str(start);
   searchst=['_000' num];
if start>=10 & start<100
   num=int2str(start);
   searchst=[' 00' num];
if start>=100 & start<1000
   num=int2str(start);
   searchst=[' 0' num];
end
if start>=1000
   num=int2str(start);
   searchst=['_' num];
end
filename=filenamestart;
n=start;
for (n=start:stop)
   if n<10
       num=int2str(n);
       replacest=['_000' num];
   end
   if n \ge 10 \& n < 100
       num=int2str(n);
       replacest=[' 00' num];
   if n \ge 100 \& n < 1000
       num=int2str(n);
       replacest=[' 0' num];
   end
   if n > = 1000
       num=int2str(n);
       replacest=['_' num];
```

```
end
    filename=strrep(filenamestart, searchst, replacest);
    getfftcsv(filename, ['FFT' strrep(filename, 'csv', 'txt')], 2);
    if n==stop
        getfftcsv(filename, ['FFT' strrep(filename, 'csv', 'txt')], 1)
    end
%this is where we will be prompted to enter the range interested
range=input('enter range [freqmin, freqmax]'); %adjust range of %FFT data
%start to do the lorentzian fits one after the next
filename=filenamestart;
for (n=start:stop)
    if n<10
        num=int2str(n);
       replacest=[' 000' num];
    end
    if n \ge 10 \& n < 100
       num=int2str(n);
       replacest=[' 00' num];
    end
    if n \ge 100 \& n < 1000
       num=int2str(n);
       replacest=[' 0' num];
    if n > = 1000
       num=int2str(n);
        replacest=['_' num];
    end
    filename=strrep(filenamestart, searchst, replacest);
    filename=['FFT' filename];
    filename=strrep(filename, 'csv', 'txt');
    [x0(1,n+1) Q(1,n+1) w(1,n+1) y0(1,n+1) R(1,n+1)]=fitlorentzianmultiple(filename,
range, 1);
end
%these lines of code dump my fitted parameters to a TXT file as a %tab delimited
output=[x0' Q' w' y0' R'];
dlmwrite(savename,output, '\t')
function null=getfft(filename, savename, mode)
%this function takes the CSV file outputted from the ocilliscope
%and takes the FFT of the data.
%modes
\ensuremath{\,^{8}0}\xspace^{-} plots ffT, doesnt save a file
%1-plots data, plots FFT, saves file
%2-only saves the FFT, no plots
data=csvread(filename);
samples=data(1,2);
t=data(2,2);
T=t*samples;
```

```
trace=data(:,5);
for(i=1:length(trace))
    if (isnan(trace(i,1)))
       if i==1
           trace(i, 1) = 0;
           trace(i,1) = (trace(i-1,1));
        end
    end
end
if (mode \sim = 2)
    figure
    plot(trace)
end
y=fft(trace);
X=[0 : (length(y) - 1)]*(1/T);
if (mode \sim = 2)
figure
plot(X,X.*abs(y'))
if (mode~=0)
    output=[X', (X.*abs(y'))'];
    dlmwrite(savename, output, '\t')
end
function [x0 Q w y0 R]=fitlorentzianmultiple(filename, range, mode)
%Fit me a lorentzian! This program will take my FFT and fit it based
%on a range to a lorentzian. The program uses the range as input and
%calculates intelligent starting initial conditions for the fitting routine
%Import filename in a manner such that frequency data is the first column
%the magnitude data should be in the second column. it needs to be tab
%delimited
%mode 1 - single lorentzian
%mode 2 - double lorentzian
fftdata=importdata(filename,'\t');
%range=input('enter range [freqmin, freqmax]'); %adjust range of FFT data
if mode==2
centerfreq=input('enter midpoint between peaks');
%find the indexes that correspond to the max and min in the data
minindex=find(fftdata>=range(1,1));
minindex=minindex(1,1);
maxindex=find(fftdata>=range(1,2));
maxindex=maxindex(1,1);
%keep only the data within the bounds
xdata=fftdata(minindex:maxindex,1);
ydata=fftdata(minindex:maxindex,2);
%initialize inits initial conditions
inits=[1, 1, 1, 1, 2, 2, 2, 2, 2];
%mode 1 - single lorentzian
```

```
if mode==1
           lorentzian=fittype ('(y0+A/(w*pi*(1+((x-x0)/w)^2)))');
           %different fitting function, (w is HWHM)
           %w is FWHM
           %x0 is the centerpoint
           \mbox{\ensuremath{\$A}} is area under peak not including the offset y0
           %y0 is the DC offset
          %assume y0 is minimum in the dataset
          y0min=min(ydata);
          inits (1, 4) = y0min;
          %inits(1,1)=max(ydata)-y0min;
           %compute the area under the plot by subtracting the y0 area from the
           %integral under the curve
          area=trapz(xdata,ydata);
          area offset = y0min*(abs(range(1,1)-range(1,2)));
          aa=area-areaoffset;
          inits(1,1) = area - area offset;
          %find the centroid x0 by taking the derivitive and then approximating
           %the zero
          diffy=gradient(ydata);
          indexleft=find(diffy==max(diffy));
          indexright=find(diffy==min(diffy));
          inits (1,3) = (xdata(indexleft(1,1),1) + xdata(indexright(1,1),1))/2;
          %use centroid and y0 to find the FWHM
          halfheight=(max(ydata)-y0min)/2;
          halfwidthx=find(ydata>=halfheight);
          halfwidthx=xdata(halfwidthx(1,1),1);
          hwhm=(inits(1,3)-halfwidthx);
          inits (1, 2) = hwhm;
                      %inits(1,1)
          %inits(1,2)
           %inits(1,3)
          %inits(1,4)
          opts
fitoptions('method','NonlinearLeastSquares','StartPoint',[inits(1,1),inits(1,2),inits(
1,3), inits(1,4)]);
           [fresult, gof, fitoutput] = fit (xdata, ydata, lorentzian, opts);
          format long;
          qof;
          x0=fresult.x0;
          y0=fresult.y0;
          A=fresult.A;
          w=fresult.w;
          Q=x0/(2*w);
          R=qof.rsquare;
          plot(fresult,xdata,ydata,'fit')
          xlabel('Frequency (Hz)')
          ylabel('Amplitude (A.U.)')
           title('Plot of Lorentzian fit with data points')
          plotrange=axis;
          axis([min(xdata),max(xdata),plotrange(1,3),plotrange(1,4)]);
          plotrange=axis;
          \texttt{text}\,(\texttt{plotrange}\,(1,1) + (\texttt{plotrange}\,(1,2) - \texttt{plotrange}\,(1,1)) \,/\, 30, \texttt{plotrange}\,(1,4) - 1) \, \text{text}\,(\texttt{plotrange}\,(1,4) + (\texttt{plotrange}\,(1,4) - 1)) \,/\, 30, \texttt{plotrange}\,(1,4) - 1) \, \text{text}\,(\texttt{plotrange}\,(1,4) + (\texttt{plotrange}\,(1,4) - 1)) \,/\, 30, \texttt{plotrange}\,(1,4) - 1) \, \text{text}\,(\texttt{plotrange}\,(1,4) - 1) \,) \, \text{text}\,(\texttt{plotrange}\,(1,4) - 1) \,) \,) \,) \,
(plotrange(1,4)-plotrange(1,3))/6, sprintf('R^2 = %f nf 0 = %e Hz nw = %e nQ {appx} = %e nQ 
%f\n', gof.rsquare, fresult.x0, fresult.w, Q));
```

```
else
```

```
('(y0+A0/(w0*pi*(1+((x-x0)/w0)^2))+y1+A1/(w1*pi*(1+((x-x0)/w0)^2))+y1+A1/(w1*pi*(1+((x-x0)/w0)^2))+y1+A1/(w1*pi*(1+((x-x0)/w0)^2))+y1+A1/(w1*pi*(1+((x-x0)/w0)^2))+y1+A1/(w1*pi*(1+((x-x0)/w0)^2))+y1+A1/(w1*pi*(1+((x-x0)/w0)^2))+y1+A1/(w1*pi*(1+((x-x0)/w0)^2))+y1+A1/(w1*pi*(1+((x-x0)/w0)^2))+y1+A1/(w1*pi*(1+((x-x0)/w0)^2))+y1+A1/(w1*pi*(1+((x-x0)/w0)^2))+y1+A1/(w1*pi*(1+((x-x0)/w0)^2))+y1+A1/(w1*pi*(1+((x-x0)/w0)^2))+y1+A1/(w1*pi*(1+((x-x0)/w0)^2))+y1+A1/(w1*pi*(1+((x-x0)/w0)^2))+y1+A1/(w1*pi*(1+((x-x0)/w0)^2))+y1+A1/(w1*pi*(1+((x-x0)/w0)^2))+y1+A1/(w1*pi*(1+((x-x0)/w0)^2))+y1+A1/(w1*pi*(1+((x-x0)/w0)^2))+y1+A1/(w1*pi*(1+((x-x0)/w0)^2))+y1+A1/(w1*pi*(1+((x-x0)/w0)^2))+y1+A1/(w1*pi*(1+((x-x0)/w0)^2))+y1+A1/(w1*pi*(1+((x-x0)/w0)^2))+y1+A1/(w1*pi*(1+((x-x0)/w0)^2))+y1+A1/(w1*pi*(1+((x-x0)/w0)^2))+y1+A1/(w1*pi*(1+((x-x0)/w0)^2))+y1+A1/(w1*pi*(1+((x-x0)/w0)^2))+y1+A1/(w1*pi*(1+((x-x0)/w0)^2))+y1+A1/(w1*pi*(1+((x-x0)/w0)^2))+y1+A1/(w1*pi*(1+((x-x0)/w0)^2))+y1+A1/(w1*pi*(1+((x-x0)/w0)^2))+y1+A1/(w1*pi*(1+((x-x0)/w0)^2))+y1+A1/(w1*pi*(1+((x-x0)/w0)^2))+y1+A1/(w1*pi*(1+((x-x0)/w0)^2))+y1+A1/(w1*pi*(1+((x-x0)/w0)^2))+y1+A1/(w1*pi*(1+((x-x0)/w0)^2))+y1+A1/(w1*pi*(1+((x-x0)/w0)^2))+y1+A1/(w1*pi*(1+((x-x0)/w0)^2))+y1+A1/(w1*pi*(1+((x-x0)/w0)^2))+y1+A1/(w1*pi*(1+((x-x0)/w0)^2))+y1+A1/(w1*pi*(1+((x-x0)/w0)^2))+y1+A1/(w1*pi*(1+((x-x0)/w0)^2))+y1+A1/(w1*pi*(1+((x-x0)/w0)^2))+y1+A1/(w1*pi*(1+((x-x0)/w0)^2))+y1+A1/(w1*pi*(1+((x-x0)/w0)^2))+y1+A1/(w1*pi*(1+((x-x0)/w0)^2))+y1+A1/(w1*pi*(1+((x-x0)/w0)^2))+y1+A1/(w1*pi*(1+((x-x0)/w0)^2))+y1+A1/(w1*((x-x0)/w0)^2)+y1+A1/(w1*((x-x0)/w0)^2)+y1+A1/(w1*((x-x0)/w0)^2)+y1+A1/(w1*((x-x0)/w0)^2)+y1+A1/(w1*((x-x0)/w0)^2)+y1+A1/(w1*((x-x0)/w0)^2)+y1+A1/(w1*((x-x0)/w0)^2)+y1+A1/(w1*(x-x0)/w0)+y1+A1/(w1*(x-x0)/w0)+y1+A1/(w1*(x-x0)/w0)+y1+A1/(w1*(x-x0)/w0)+y1+A1/(w1*(x-x0)/w0)+y1+A1/(w1*(x-x0)/w0)+y1+A1/(w1*(x-x0)/w0)+y1+A1/(w1*(x-x0)/w0)+y1+A1/(w1*(x-x0)/w0)+y1+A1/(w1*(x-x0)/w0)+y1+A1/(w1*(x-x0)/w0)+y1+A1/(w1*(x-x0)/w0)+y1+A1/(w1*(x-x0)/w0)+y1+A1/(w1*(x-x0)/w0)+y1+A1/(w1*(x-x0)/w0)+w1+A1/(w1*(x-x0
        dbllorentzian=fittype
x1)/w1)^2)))') %different fitting function (w is HWHM)
        %w0 is FWHM of left peak
        %x0 is the centerpoint for left peak
        %AO is area under left peak not including the offset yO
        %y0 is the DC offset for left peak
        %w1 is FWHM of right peak
        %x1 is the centerpoint for right peak
        %Al is area under peak not including the offset y0 and x0
        %y1 is the DC offset for right peak
        maxindex=size(xdata);
        maxindex=maxindex(1,1);
        halfrange=(centerfreq);
        halfindex=find(xdata>=halfrange);
        halfindex=halfindex(1,1);
        figure
\verb|plot(xdata(1:halfindex,1),ydata(1:halfindex,1),'r',xdata(halfindex:maxindex,1),ydata(halfindex)|\\
alfindex:maxindex,1),'b')
        %assume y0 is first point of dataset on left
        y0min=ydata(1,1);
        inits(1,7) = y0min;
        %assume y1 is first point of dataset on right
        ind=size(ydata);
        y1min=ydata(ind(1,1),1);
        inits (1, 8) = y0min;
        %compute the area under the left half of the plot by subtracting the y0 area from
        %integral under the curve
        area0=trapz(xdata(1:halfindex,1),ydata(1:halfindex,1));
        areaoffset0=y0min*(abs(range(1,1)-halfrange));
        inits(1,1) = area0 - areaoffset0;
        areal=trapz(xdata(halfindex:maxindex,1),ydata(halfindex:maxindex,1));
        areaoffset1=y1min*(abs(halfrange-range(1,2)));
        inits(1,2) = area1 - areaoffset1;
        %find the centroid x0 by taking the dnerivitive and then approximating
        %the zero
        maximumy0=max(ydata(1:halfindex,1));
        indexleft=find(ydata==maximumy0);
        xdata(indexleft(1,1),1);
        inits(1,5) = xdata(indexleft(1,1),1);
        maximumy1=max(ydata(halfindex:maxindex,1));
        indexright=find(ydata==maximumy1);
        xdata(indexright(1,1),1);
        inits(1,6) = xdata(indexright(1,1),1);
        %use centroid and y0 to find the {\tt FWHM}
        halfheight=(maximumy0-y0min)/2;
        halfwidthx=find(ydata>=halfheight);
        hindx=size(halfwidthx);
        halfwidthx=xdata(halfwidthx(1,1),1)
        hwhm0=abs(inits(1,5)-halfwidthx);
        inits (1,3) = hwhm0;
        halfheight=(maximumy1-y1min)/2;
        halfwidthx=find(ydata>=halfheight);
        halfwidthx=xdata(halfwidthx(1,1),1);
```

```
hwhm1=abs((inits(1,6)-halfwidthx));
    inits(1,4)=hwhm1;
    opts
fitoptions ('method', 'NonlinearLeastSquares', 'StartPoint', [inits(1,1),inits(1,2),inits(
1,3), inits(1,4), inits(1,5), inits(1,6), inits(1,7), inits(1,8)]);
    [fresult,gof,fitoutput]=fit(xdata,ydata,dbllorentzian,opts);
    gof
    fresult
    %x0=fresult.x0
    %y0=fresult.y0
    %A=fresult.A
    %w=fresult.w
    %xfit=xdata;
    %yfit=d+a./((xdata-b).^2+c^2);
    figure
    plot(fresult, xdata, ydata, 'fit')
   xlabel('Frequency (Hz)')
ylabel('Amplitude (A.U.)')
    title('Plot of Lorentzian fit with data points')
    text(min(xdata), max(ydata), sprintf('x_0 = %f', fresult.x0));
end
```

Bibliography

- [1] T. J. Suleski and R. D. T. Kolste, "Fabrication trends for free-space microoptics," *Journal of Lightwave Technology*, vol. 23, pp. 633, 2005.
- [2] K. E. Petersen, "Silicon as a mechanical material," *Proceedings of the IEEE*, vol. 70, pp. 420, 1982.
- [3] H. Fujita and H. Toshiyoshi, "Optical MEMS," *IEICE Trans. Elec.*, vol. E83, pp. 1427-1434, 2000.
- [4] D. J. Bishop, C. R. Giles, and G. P. Austin, "The Lucent LambdaRouter: MEMS technology of the future here today," *IEEE Commun. Mag.*, vol. 40, pp. 75-79, 2002.
- [5] P. B. Chu, I. Brener, C. Pu, S.-S. Lee, J. I. Dadap, S. Park, K. Bergman, N. H. Bonadeo, T. Chau, M. Chou, R. A. Doran, R. Gibson, R. Harel, J. J. Johnson, C. D. Lee, D. R. Peale, B. Tang, D. T. K. Tong, M.-J. Tsai, Q. Wu, W. Zhong, E. L. Goldstein, L. Y. Lin, and J. A. Walker, "Design and Nonlinear Servo Control of MEMS Mirrors and Their Performance in a Large Port-Count Optical Switch," *Journal of Microelectromechanical Systems*, vol. 14, pp. 261-273, 2005.
- [6] L. J. Hornbeck, "Current status of the digital micromirror device (DMD) for projection television applications," in *International Electron Devices Meeting 1993. Technical Digest* (Cat. No.93CH3361-3). New York, NY: IEEE Electron Devices Soc. IEEE, 1993, pp. 381.
- [7] http://www.dlp.com/dlp_technology, "Texas Instruments' DLP Technology: Digital Light Processing for DLP Projection," December 1, 2003.
- [8] L. Y. Lin, E. L. Goldstein, and R. W. Tkach, "Free-space micromachined optical switches for optical networking," *IEEE Journal of Selected Topics in Quantum Electronics*, vol. 5, pp. 4-9, 1999.
- [9] T. G. McDonald and L. A. Yoder, "Digital micromirror devices make projection displays," *Laser Focus World*, vol. 33, pp. SUPL5-8, 1997.
- [10] D. T. Neilson, R. Frahm, P. Kolodner, C. A. Bolle, R. Ryf, J. Kim, A. R. Papazian, C. J. Nuzman, A. Gasparyan, N. R. Basavanhally, V. A. Aksyuk, and J. V. Gates, "256 256 Port

- Optical Cross-Connect Subsystem," *Journal of Lightwave Technology*, vol. 22, pp. 1499-1509, 2004.
- [11] G. N. Nielson, D. Seneviratne, F. Lopez-Royo, P. T. Rakich, F. Giacometti, H. L. Tuller, and G. Barbastathis, "MEMS based wavelength selective optical switching for integrated photonic circuits," presented at Conference on Lasers and Electro-Optics (CLEO), San Francisco, CA, 2004.
- [12] M. Xiaohua, "Optical switching technology comparison: optical MEMS vs. other technologies," *IEEE communications magazine*, vol. 41, pp. S16, 2003.
- [13] E. Ollier, "Optical MEMS devices based on moving waveguides," *IEEE Journal on Selected Topics in Quantum Electronics*, vol. 8, pp. 155-162, 2002.
- [14] T. Bakke, C. P. Tigges, J. J. Lean, C. T. Sullivan, and O. B. Spahn, "Planar microoptomechanical waveguide switches," *IEEE Journal of Selected Topics in Quantum Electronics*, vol. 8, pp. 64-72, 2002.
- [15] M. W. Pruessner, N. Siwak, K. Amarnath, S. Kanakaraju, W.-H. Chuang, and R. Ghodssi, "End-coupled Optical waveguide MEMS Devices in the Indium Phosphide Material System," *Journal of Micromechanics and Microengineering (JMM)*, vol. 16, pp. 832-842, 2006.
- [16] P. Kumar, L. Lihua, L. Calhoun, P. Boudreaux, and D. DeVoe, "Fabrication of piezoelectric Al/sub 0.3/Ga/sub 0.7/As microstructures," *Sensors and Actuators A (Physical)*, vol. A115, pp. 96, 2004.
- [17] K. Rottner, R. Helbig, and G. Muller, "Piezoelectric constant of InP," *Applied Physics Letters*, vol. 62, pp. 352.
- [18] J. Soderkvist and K. Hjort, "Flexural vibrations in piezoelectric semi-insulating GaAs," Sensors and Actuators A (Physical), vol. A39, pp. 133.
- [19] H. Yamaguchi, S. Miyashita, and Y. Hirayama, "Microelectromechanical displacement sensing using InAs/AlGaSb heterostructures," *Applied Physics Letters*, vol. 82, pp. 394, 2003.
- [20] E. A. Sovero, Y. Kwon, D. S. Deakin, and J. Hong, "Watt level GaAs PHEMT power amplifiers 26 GHz and 40 GHz for wireless applications," in *RAWCON 99. 1999 IEEE Radio and Wireless Conference (Cat. No.99EX292)*. Piscataway, NJ: IEEE, 1999, pp. 309.

- [21] H. L. Hartnagel, K. Mutamba, J. Pfeiffer, R. Riemenschneider, and J. Peerlings, "MEMS based on III-V compounds for sensing applications and optical communications," presented at Annual Device Research Conference, 1999.
- [22] E. F. Schubert, "Physical Foundations of Solid-State Devices," 2006.
- [23] M. W. Pruessner, K. Amarnath, M. Datta, D. Kelly, S. Kanakaraju, P.-T. Ho, and R. Ghodssi, "InP-Based Optical Waveguide MEMS Switches with Evanescent Coupling Mechanism," *Journal of Microelectromechanical Systems*, vol. 14, pp. 1070-81, 2005.
- [24] M. Datta, M. W. Pruessner, K. Amarnath, J. McGee, S. Kanakaraju, and R. Ghodssi, "Wavelength-Selective Integrated Optical MEMS Filter in InP," presented at 18th International Conference on Micro Electro Mechanical Systems, Miami Beach, FL, 2005.
- [25] S. Irmer, J. Daleiden, V. Rangelov, C. Prott, F. Römer, M. Strassner, A. Tarraf, and H. Hillmer, "Ultralow Biased Widely Continuously Tunable Fabry–Pérot Filter," *IEEE Photonics Technology Letters*, vol. 15, pp. 434-436, 2003.
- [26] A. Lipson and E. M. Yeatman, "Free-space MEMS tunable optical filter on (110) silicon," in *IEEE/LEOS Optical MEMs 2005 (IEEE Cat. No. 05EX1115)*. Piscataway, NJ: IEEE, 2005, pp. 73.
- [27] D. Sadot and E. Boimovich, "Tunable optical filters for dense WDM networks," *IEEE Communications Magazine*, vol. 36, pp. 50, 1998.
- [28] T. Zhou, D. O. Lopez, M. E. Simon, F. Pardo, V. A. Aksyuk, and D. T. Neilson, "MEMS-based 14 GHz resolution dynamic optical filter," *Electronics Letters*, vol. 39, pp. 1744, 2003.
- [29] R. T. Howe and R. S. Muller, "Resonant microbridge vapor sensor," *IEEE Transactions on Electron Devices*, vol. ED-33, pp. 499-506, 1986.
- [30] H. C. Nathanson, W. E. Newell, R. A. Wickstrom, and R. J. J. Davis, "The resonant gate transistor," *IEEE Transactions on Electron Devices*, vol. ED-14, pp. 117-133, 1967.
- [31] E. S. Snow, F. K. Perkins, E. J. Houser, S. C. Badescu, and T. L. Reinecke, "Chemical detection with a single-walled carbon nanotube capacitor," *Science*, vol. 307, pp. 1942-5.
- [32] M. C. Horrillo, J. Lozano, M. J. Fernandez, J. L. Fontecha, M. Aleixandre, J. P. Santos, I. Sayago, T. Arroyo, J. M. Cabellos, and F. J. Gutierrez, "Wine classification with a zinc

- oxide SAW sensor array," Sensors and Actuators B (Chemical), vol. 120, pp. 166-171, 2006.
- [33] N. V. Lavrik, M. J. Sepaniak, and P. G. Datskosa, "Cantilever transducers as a platform for chemical and biological sensors," *Review of Scientific Instruments*, vol. 75, pp. 2229-53, 2004.
- [34] C. K. Ho, L. K. McGrath, C. E. Davis, M. L. Thomas, J. L. Wright, A. S. Kooser, and R. C. Hughes, "Chemiresistor Microsensors for In-Situ Monitoring of Volatile Organic Compounds: Final LDRD Report," Sandia National Laboratories September 2003.
- [35] O. V. Anisimov, V. I. Gaman, N. K. Maksimova, S. M. Mazalov, and E. V. Chernikov, "Electrical and gas-sensitive properties of a resistive thin-film sensor based on tin dioxide," *Semiconductors*, vol. 40, pp. 704, 2006.
- [36] T. J. Fawcett, J. T. Wolan, R. L. Myers, J. Walker, and S. E. Saddow, "Wide-range (0.33%-100%) 3C-SiC resistive hydrogen gas sensor development," *Applied Physics Letters*, vol. 85, pp. 416, 2004.
- [37] J. Garcia-Canton, A. Merlos, and A. Baldi, "High-quality factor electrolyte insulator silicon capacitor for wireless chemical sensing," *IEEE Electron Device Letters*, vol. 28, pp. 27, 2007.
- [38] R. Igreja and C. J. Dias, "Dielectric response of interdigital chemocapacitors: The role of the sensitive layer thickness," *Sensors and Actuators B (Chemical)*, vol. 115, pp. 69, 2006.
- [39] C. Moldovan, R. Iosub, A. Tomescu, and M. Bercu, "Micromachined chemoresistive sensors for CO and CH/sub 4/ detection," in 2004 International Semiconductor Conference.

 CAS 2004 Proceedings (IEEE Cat. No.04TH8748). Piscataway, NJ: IEEE, 2004, pp. 275.
- [40] C. Moldovan, S. Sosin, O. Nedelcu, U. Kaufmann, H. J. Ritzhaupt-Kleissl, S. Dimov, P. Petkov, R. Dorey, K. Persson, D. Gomez, and P. Johander, "Chemoresistive gas sensor manufacturing using mixed technologies," in 2005 International Semiconductor Conference (IEEE Cat. No. 05TH8818), vol. vol. 1. Piscataway, NJ: IEEE, 2005, pp. 201.
- [41] S. J. Ippolito, A. Ponzoni, K. Kalantar-Zadeh, W. Wlodarski, E. Comini, G. Faglia, and G. Sberveglieri, "Layered WO/sub 3//ZnO/36° LiTaO/sub 3/ SAW gas sensor sensitive towards ethanol vapour and humidity," *Sensors and Actuators B (Chemical)*, vol. 117, pp. 442-450, 2006.

- [42] "Prime Photonics," http://www.primephotonics.com.
- [43] "Photon Technology International, Inc.," http://www.pti-nj.com.
- [44] J. M. Corres, F. J. Arregui, and I. R. Matias, "Design of humidity sensors based on tapered optical fibers," *Journal of Lightwave Technology*, vol. 24, pp. 4329, 2006.
- [45] A. Cusano, A. Iadicicco, S. Campopiano, A. Cutolo, and M. Giordano, "Self temperature referenced refractive index sensor by non-uniform thinned fiber Bragg gratings," *Sensors and Actuators B (Chemical)*, vol. 120, pp. 231, 2006.
- [46] M. A. Haidekker, W. J. Akers, D. Fischer, and E. A. Theodorakis, "Optical fiber-based fluorescent viscosity sensor," *Optics Letters*, vol. 31, pp. 2529, 2006.
- [47] S. Li-Yang, A. P. Zhang, L. Wei-Sheng, F. Hong-Yan, and H. Sailing, "Optical refractive-index sensor based on dual fiber-Bragg gratings interposed with a multimode-fiber taper," *IEEE Photonics Technology Letters*, vol. 19, pp. 30, 2007.
- [48] D. Yixiang and C. Wenqing, "Optical fiber-based evanescent ammonia sensor," *Sensors and Actuators B (Chemical)*, vol. 110, pp. 252, 2005.
- [49] R. Berger, C. Gerber, H. P. Lang, and J. K. Gimzewski, "Micromechanics: a toolbox for femtoscale science: "Towards a laboratory on a tip"," *Microelectronic Engineering*, vol. 35, pp. 373-379, 1997.
- [50] B. Illic, D. Czaplewski, M. Zalalutdinov, H. G. Craighead, P. Neuzil, C. Campagnolo, and C. Batt, "Single cell detection with micromechanical oscillators," *Journal of Vacuum Science and Technology*, vol. B19, pp. 2825-8, 2001.
- [51] B. Illic, H. G. Craighead, S. Krylov, W. Senaratne, and C.Ober, "Attogram Detection using Nanoelectromechanical Oscillators," *J. Applied Physics*, vol. 95, pp. 3694-703, 2004.
- [52] F. M. Battiston, J. P. Ramseyer, H. P. Lang, M. K. Baller, C. Gerber, J. K. Gimzewski, E. Meyer, and H. J. Guntherodt, "A chemical sensor based on a microfabricated cantilever array with simultaneous resonance-frequency and bending readout," Switzerland, 2001.
- [53] E. Forsen, G. Abadal, S. Ghatnekar-Nilsson, J. Teva, J. Verd, R. Sandberg, W. Svendsen, F. Perez-Murano, J. Esteve, E. Figueras, F. Campabadal, L. Montelius, N. Barniol, and A. Boisen, "Ultrasensitive mass sensor fully integrated with complementary metal-oxide-semiconductor circuitry," *Applied Physics Letters*, vol. 87, pp. 43507-1-3, 2005.

- [54] H. P. Lang, M. K. Baller, F. M. Battiston, J. Fritz, R. Berger, J. P. Ramseyer, P. Fornaro, E. Meyer, H. J. Guntherodt, J. Brugger, U. Drechsler, H. Rothuizen, M. Despont, P. Vettiger, C. Gerber, and J. K. Gimzewski, "The nanomechanical NOSE," in *Technical Digest. IEEE International MEMS 99 Conference. Twelfth IEEE International Conference on Micro Electro Mechanical Systems (Cat. No.99CH36291)*. Piscataway, NJ: IEEE, 1999, pp. 9.
- [55] L. A. Pinnaduwage, V. Boiadjiev, J. E. Hawk, and T. Thundat, "Sensitive detection of plastic explosives with self-assembled monolayer-coated microcantilevers," *Applied Physics Letters*, vol. 83, pp. 1471-3, 2003.
- [56] S. Dohn, R. Sandberg, W. Svendsen, and A. Boisen, "Enhanced functionality of cantilever based mass sensors using higher modes and functionalized particles," presented at The 13th International Conference on Solid-State Sensors, Actuators and Microsystems (Transducers), Seoul, South Korea, 2005.
- [57] N. V. Lavrik and P. G. Datskosa, "Femtogram mass detection using photothermally actuated nanomechanical resonators," *Applied Physics Letters*, vol. 82, pp. 2697-9, 2003.
- [58] B. Ilic, S. Krylov, K. Aubin, R. Reichenbach, and H. G. Craighead, "Optical excitation of nanoelectromechanical oscillators," *Applied Physics Letters*, vol. 86, pp. 193114-1-3, 2005.
- [59] Y. Lee, G. Lim, and W. Moon, "A self-excited micro cantilever biosensor actuated by PZT using the mass micro balancing technique," *Sensors and Actuators A (Physical)*, vol. 130-131, pp. 105-110, 2006.
- [60] P. Li and X. Li, "A single-sided micromachined piezoresistive SiO/sub 2/ cantilever sensor for ultra-sensitive detection of gaseous chemicals," *Journal of Micromechanics and Microengineering*, vol. 16, pp. 2539-2546, 2006.
- [61] K. Zinoviev, C. Dominguez, J. A. Plaza, V. J. C. Busto, and L. M. Lechuga, "A Novel Optical Waveguide Microcantilever Sensor for the Detection of Nanomechanical Forces," *Journal of Lightwave Technology*, vol. 24, pp. 2132 - 2138, 2006.
- [62] E. Ollier, P. Philippe, C. Chabrol, and P. Mottier, "Micro-opto-mechanical vibration sensor integrated on silicon," *Journal of Lightwave Technology*, vol. 17, pp. 26-29, 1999.
- [63] M. F. Mabrook, C. Pearson, and M. C. Petty, "Inkjet-printed polymer films for the detection of organic vapors," *IEEE Sensors Journal*, vol. 6, pp. 1435-1444, 2006.

- [64] Y.-H. Kim, K. Jang, Y. J. Yoon, and Y.-J. Kim, "A novel relative humidity sensor based on microwave resonators and a customized polymeric film," *Sensors and Actuators B*, vol. 117, pp. 315-322, 2006.
- [65] F. Lochon, L. Fadel, I. Dufour, D. Rebière, and J. Pistré, "Silicon made resonant microcantilever- Dependence of the chemical sensing performances on the sensitive coating thickness," *Materials Science and Engineering C*, vol. 26, pp. 348-353, 2006.
- [66] I. Voiculescu, M. E. Zaghloul, R. A. McGill, E. J. Houser, and G. K. Fedder, "Electrostatically Actuated Resonant Microcantilever Beam in CMOS Technology for the Detection of Chemical Weapons," *IEEE Sensors Journal*, vol. 5, pp. 641-647, 2005.
- [67] C. Bartic, B. Palan, A. Campitelli, and G. Borghs, "Monitoring pH with organic-based field-effect transistors," Switzerland, 2002.
- [68] B. Crone, A. Dodabalapur, A. Gelperin, L. Torsi, H. E. Katz, A. J. Lovinger, and Z. Bao, "Electronic sensing of vapors with organic transistors," *Applied Physics Letters*, vol. 78, pp. 2229-2231, 2001.
- [69] L. Torsi, "Novel applications of organic based thin film transistors," UK, 2000.
- [70] L. Torsi, A. Dodabalapur, L. Sabbatini, and P. G. Zambonin, "Multi-parameter gas sensors based on organic thin-film-transistors," *Sensors and Actuators B (Chemical)*, vol. B67, pp. 312, 2000.
- [71] J. N. Zemel, "Ion sensitive field effect transistors and related devices," *Analytical Chemistry*, vol. 47, pp. 255A, 258-9, 264-5, 268, 1975.
- [72] H. G. Bach, A. Beling, G. G. Mekonnen, R. Kunkel, D. Schmidt, W. Ebert, A. Seeger, M. Stollberg, and W. Schlaak, "InP-based waveguide-integrated photodetector with 100-GHz bandwidth," *IEEE Journal of Selected Topics in Quantum Electronics*, vol. 10, pp. 668, 2004.
- [73] A. Umbach, D. Trommer, G. G. Mekonnen, W. Ebert, and G. Unterborsch, "Waveguide integrated 1.55 um photodetector with 45 GHz bandwidth," *Electronics Letters*, vol. 32, pp. 2143, 1996.
- [74] N. Emeis, M. Schier, L. Hoffmann, H. Heinecke, and B. Baur, "High speed waveguide-integrated photodiodes grown by metal organic molecular beam epitaxy," *Electronics Letters*, vol. 28, pp. 344, 1992.

- [75] K. Kato and Y. Akatsu, "High-speed waveguide photodetectors," in *Conference Proceedings. Seventh International Conference on Indium Phosphide and Related Materials (Cat. No.95CH35720)*. New York, NY: IEEE Japan Soc. Appl. Physics, 1995, pp. 349.
- [76] D. Trommer, G. Unterborsch, D. Schumann, O. Reimann, D. Huhse, and D. Bimberg, "Above 100 GHz performance of waveguide integrated photodiodes measured by electrooptical sampling," in 2003 International Conference Indium Phosphide and Related Materials. Conference Proceedings (Cat. No.03CH37413). Piscataway, NJ: IEEE, 2003, pp. 164.
- [77] K. S. Giboney, R. L. Nagarajan, T. E. Reynolds, S. T. Allen, R. P. Mirin, M. J. W. Rodwell, and J. E. Bowers, "Travelling-wave photodetectors with 172-GHz bandwidth and 76-GHz bandwidth-efficiency product," *IEEE Photonics Technology Letters*, vol. 7, pp. 412, 1995.
- [78] K. S. Giboney, J. W. Rodwell, and J. E. Bowers, "Traveling-wave photodetector theory," *IEEE Transactions on Microwave Theory and Techniques*, vol. 45, pp. 1310, 1997.
- [79] S.-H. Lim, D. Raorane, D. Raorane, S. Satyanarayana, and A. Majumdar, "Nano-chemo-mechanical sensor array platform for high-throughput chemical analysis," *Sensors and Actuators B (Chemical)*, vol. 119, pp. 466-474, 2006.
- [80] D. Then, A. Vidic, and C. Ziegler, "A highly sensitive self-oscillating cantilever array for the quantitative and qualitative analysis of organic vapor mixtures," *Sensors and Actuators B (Chemical)*, vol. 117, pp. 1-9, 2006.
- [81] H. Hosaka, K. Itao, and S. Kuroda, "Damping characteristics of beam-shaped micro-oscillators," *Sensors and Actuators A*, vol. 49, pp. 87-95, 1995.
- [82] S. Pamidighantam, "Pull-in voltage analysis of electrostatically actuated beam structures with fixed-fixed and fixed-free end conditions," *Journal of micromechanics and microengineering*, vol. 12, pp. 458-464, 2002.
- [83] D. Marcuse, "Tilt, Offset, and End-Separation Loss of Lowest-Order Slab Waveguide Mode," *Journal of Lightwave Technology*, vol. LT-4, pp. 1647-1650, 1986.
- [84] M. W. Pruessner, "Indium Phosphide Based Optical Waveguide MEMS for Communications and Sensing," in *Electircal and Computer Engineering*. College Park, MD: University of Maryland, 2005.

- [85] D. Kelly, M. W. Pruessner, K. Amarnath, M. Datta, S. Kanakaraju, L. C. Calhoun, and R. Ghodssi, "Monolithic Suspended Optical Waveguides for InP MEMS," *IEEE Photonics Technology Letters*, vol. 16, pp. 1298-300, 2004.
- [86] R. Grover, J. H. Hryniewicz, O. S. King, and V. Van, "Process development of methane–hydrogen–argon-based deep dry etching of InP for high aspect-ratio structures with vertical facet-quality sidewalls," *Journal of Vacuum Science and Technology*, vol. B19, pp. 1071-1023, 2001.
- [87] M. W. Pruessner, "Personal Communication," 2005.
- [88] M. W. Pruessner, T. King, D. Kelly, R. Grover, L. C. Calhoun, and R. Ghodssi, "Mechanical Property Measurement of InP-based MEMS for Optical Communications," *Sensors and Actuators*, vol. A105, pp. 190-200, 2003.
- [89] M. W. Pruessner, "Toward III-V optical MEMS: mechanical property measurement of indium phosphide using nanoindentation, beam bending, and electrostatic testing methods (M. S. Thesis)," in *Department of Electrical and Computer Engineering*. College Park: University of Maryland, 2002, pp. 135.
- [90] J. H. Perkins, M. F. O. O'Keefe, R. E. Miles, and C. M. Snowden, "Pt and Zn based ohmic contacts to p-type InP," in *Conference Proceedings. Sixth International Conference on Indium Phosphide and Related Materials (Cat. No.94CH3369-6)*. New York, NY: IEEE, 1994, pp. 190.
- [91] P. Elias, J. Martaus, J. Soltys, and I. Kostic, "Micromachining of mesa and pyramidal-shaped objects in (100) InP substrates," *Journal of Micromechanics and Microengineering*, vol. 15, pp. 1007, 2005.
- [92] K. Hjort, "Sacrificial etching of III–V compounds for micromechanical devices," *Journal of Micromechanics and Microengineering*, vol. 6, pp. 370-375, 1996.
- [93] S. R. Forrest, "Ultrathin Organic Films Grown by Organic Molecular Beam Deposition and Related Techniques," *Chemical Review*, vol. 97, pp. 1793-1896, 1997.
- [94] S. P. Park, S. S. Kim, J. H. Kim, C. N. Whang, and S. Im, "Optical and luminescence characteristics of thermally evaporated pentacene films on Si," *Applied Physics Letters*, vol. 80, pp. 2872-4, 2002.

- [95] R. Ruiz, D. Choudhary, B. Nickel, T. Toccoli, C. Kee-Chul, A. C. Mayer, P. Clancy, J. M. Blakely, R. L. Headrick, S. Iannotta, and G. G. Malliaras, "Pentacene thin film growth," *Chemistry of Materials*, vol. 16, pp. 4497, 2004.
- [96] O. D. Jurchescu, J. Baas, and T. T. M. Palstra, "Electronic transport properties of pentacene single crystals upon exposure to air," *Applied Physics Letters*, vol. 87, pp. 52102-1-3, 2005.
- [97] N. Koch, J. Ghijsen, R. L. Johnson, J. Schwartz, J. J. Pireaux, and A. Kahn, "Physisorption-like interaction at the interfaces formed by pentacene and samarium," *Journal of Physical Chemistry B*, vol. 106, pp. 4192, 2002.
- [98] S. Adachi, *Physical properties of III-V semiconductor compounds*. New York: Wiley and Sons, 1992.
- [99] G. Stemme, "Resonant silicon sensors," *Journal of Micromechanics and Microengineering*, vol. 1, pp. 113, 1991.
- [100] A. Bietsch, Z. Jiayun, M. Hegner, H. P. Lang, and C. Gerber, "Rapid functionalization of cantilever array sensors by inkjet printing," *Nanotechnology*, vol. 15, pp. 873, 2004.